ACS APPLIED MATERIALS & INTERFACES

www.acsami.org

Research Article

Reactive Oxygen Species- and Cell-Free DNA-Scavenging Mn_3O_4 Nanozymes for Acute Kidney Injury Therapy

Longxiyu Meng, Jiayuan Feng, Jie Gao, Yihong Zhang, Wenjing Mo, Xiaozhi Zhao,* Hui Wei,* and Hongqian Guo*

Cite This: *ACS Appl. Mater. Interfaces* 2022, 14, 50649−50663

Read Online

ACCESS | Metrics & More | Article Recommendations | Supporting Information

ABSTRACT: Reactive oxygen species (ROS) scavenging therapy toward acute kidney injury (AKI) is promising, but no effective ROS scavenging drug has been developed yet. Moreover, cell-free DNA (cfDNA) is also involved in AKI, but the corresponding therapies have not been well developed. To tackle these challenges, Mn_3O_4 nanoflowers (Nfs) possessing both ROS and cfDNA scavenging activities were developed for better AKI protection as follows. First, Mn_3O_4 Nfs could protect HK2 cells through cascade ROS scavenging (dismutating $\cdot O_2^-$ into H_2O_2 by superoxide dismutase-like activity and then decomposing H_2O_2 by catalase-like activity). Second, Mn_3O_4 Nfs could efficiently adsorb cfDNA and then decrease the inflammation caused by cfDNA. Combined, remarkable therapeutic efficacy was achieved in both cisplatin-induced and ischemia−reperfusion AKI murine models. Furthermore, Mn_3O_4 Nfs could be used for the T_1-MRI real-time imaging of AKI. This study not only offered a promising treatment for AKI but also showed the translational potential of nanozymes.

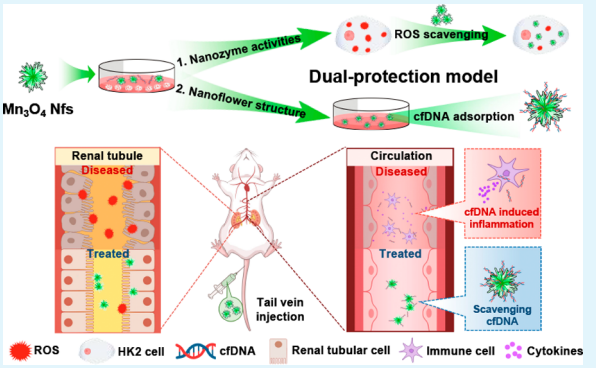

KEYWORDS: *acute kidney injury, nanozymes, Mn_3O_4 nanoflowers, reactive oxygen species, cell-free DNA*

INTRODUCTION

Acute kidney injury (AKI) is defined as a sharp decline in the glomerular filtration rate and a sudden increase in the blood nitrogen wastes.[1] AKI occurs in approximately 10−15% of hospitalized patients and more than 50% of intensive care patients,[2] which is responsible for approximately 1.7 million deaths each year worldwide with increasing severity.[3,4] Unfortunately, effective therapies for AKI are still lacking, and patients who experience severe AKI often require dialysis and even a kidney transplantation.[4,5]

Recently, numerous therapeutic strategies have been developed by exploring the pathological characteristics of AKI.[6] On the one hand, ischemia, nephrotoxins, and sepsis are the major causes of AKI, all of which are associated with the overproduction of reactive oxygen species (ROS).[7−9] The overproduced ROS leads to apoptosis and necroptosis and then promotes inflammation and causes kidney damage.[10] Antioxidants are employed to scavenge ROS and alleviate oxidative damage, such as glutathione and antioxidative enzymes (superoxide dismutase (SOD), catalase (CAT), and glutathione peroxidase (GPX)).[11,12] To date, there is no effective GSH delivery for AKI treatment. Moreover, GSH is consumed when it is used for ROS scavenging. Although antioxidative enzymes catalytically scavenge ROS, they cannot fully meet therapeutic needs because of their intrinsic limitations, such as low stability and high cost. Nanozymes, the functional nanomaterials with enzyme-like activities, have emerged as novel artificial enzymes to address the limitations of enzymes. When compared with natural enzymes, nanozymes have higher catalytic stability, ease of modification, and lower manufacturing cost. Numerous nanozymes have been employed for ROS-scavenging therapies.[13−30] Recently, a few nanozymes have been fabricated for AKI treatment by taking advantage of their sole SOD activity (Table S1).[31−36]

On the other hand, recent studies revealed that serum cell-free DNA (cfDNA) levels significantly increased in AKI mouse models and caused acute inflammation.[37] Notably, mitochondrial DNA (mtDNA) in the plasma is a source of cfDNA. The levels of mtDNA in the plasma of the platinum-treated patients were higher than those of healthy controls, and these mtDNA, as the cfDNA, exacerbated cisplatin-induced AKI.[38] Similarly, another study revealed that plasma cf-mtDNA levels increased after ischemia−reperfusion (IR) injury, which may aggravate the inflammatory response and tissue damage of IR-AKI.[39] Additionally, cfDNA has been associated with some IR

Received: September 9, 2022
Accepted: October 19, 2022
Published: November 5, 2022

Scheme 1. Schematic Representation of the Therapeutic Mechanism of Mn_3O_4 Nfs to AKI[a]

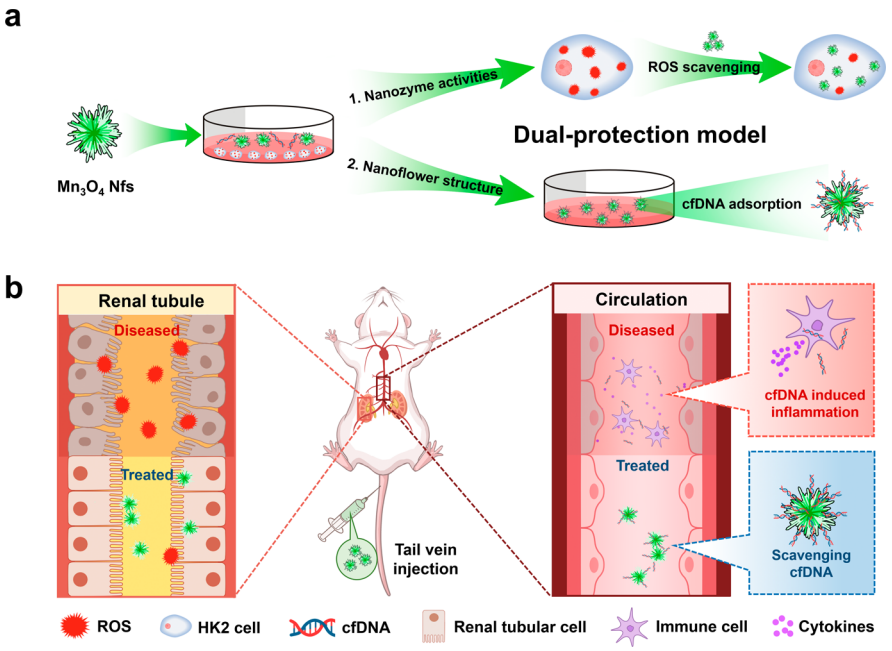

[a](a) Dual-protection models of Mn_3O_4 Nfs in vitro. (b) Protection mechanism of Mn_3O_4 Nfs for AKI by removing circulating cfDNA and scavenging excessive ROS in the kidney in vivo.

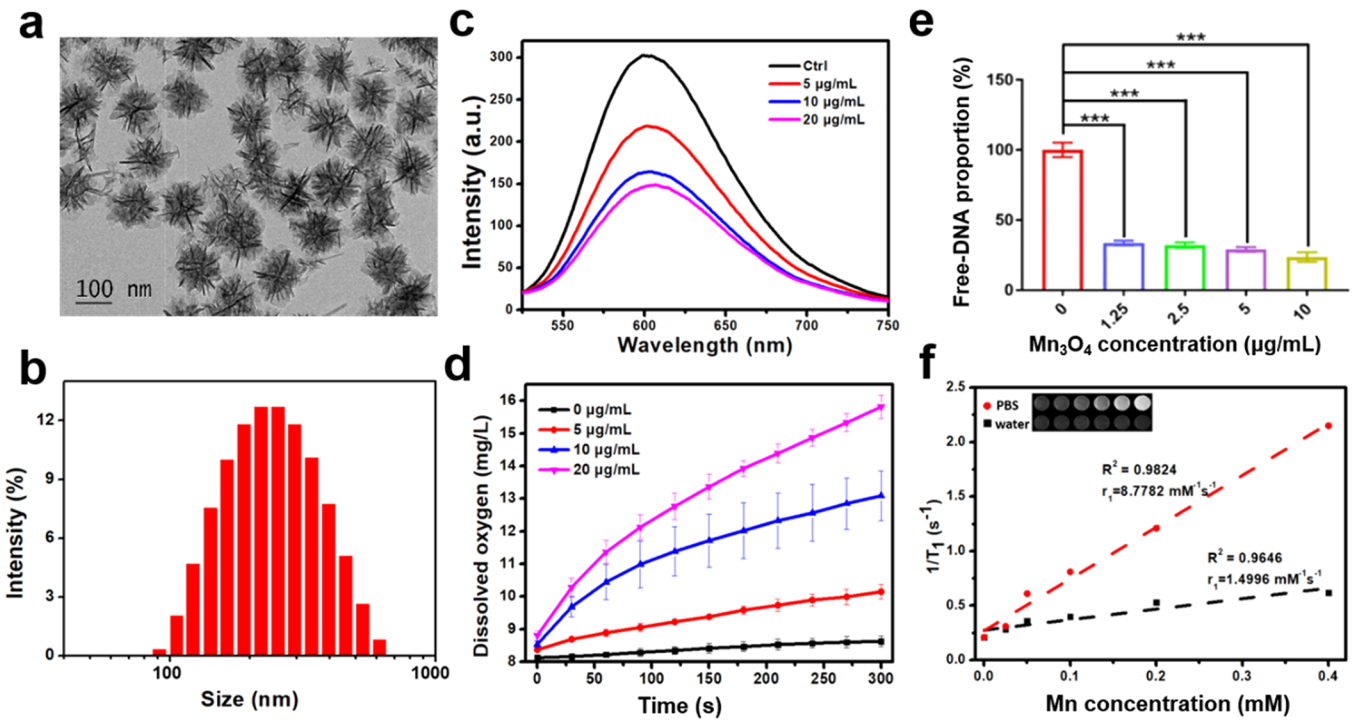

Figure 1. Characterization and properties of Mn_3O_4 Nfs. (a) TEM image of Mn_3O_4 Nfs. (b) Size distribution of Mn_3O_4 Nfs. (c) Fluorescent spectra of HE after reaction with xanthine and xanthine oxidase, in the absence and presence of different concentrations of Mn_3O_4 Nfs. The fluorescence decrease indicates the superoxide radical scavenging ability of Mn_3O_4 Nfs. (d) Typical kinetic curves of oxygen generation from the decomposition of H_2O_2 in the absence and presence of different concentrations of Mn_3O_4 Nfs (n = 4). (e) cfDNA adsorption ability of Mn_3O_4 Nfs (n = 4). (f) MRI ability of Mn_3O_4 Nfs when incubated with water and PBS. (d, e) Data are presented as mean ± SD, two-tailed Student's t-test for P values (***P < 0.001).

diseases[40,41] and has aggravated inflammation by cfDNA-mediated immune activation. Therefore, cfDNA is possibly involved in both cisplatin- and IR-induced AKI and has an intricate relationship with AKI: AKI would induce the release of cfDNA, and in turn, the released cfDNA could aggravate the AKI through the immune activation, inflammation, and oxidative stress process.[42−47] We reasoned that designing one system with both ROS and cfDNA scavenging activities could

https://doi.org/10.1021/acsami.2c16305
ACS Appl. Mater. Interfaces 2022, 14, 50649−50663

tackle these two pathological features of AKI simultaneously and would provide more effective strategies for AKI treatment. To our knowledge, such a combined therapeutic strategy has not been explored yet.

Here, we synthesized a nanoflower (Nf)-structured Mn_3O_4 with dual ROS scavenging and cfDNA adsorption capacities for the AKI treatment. Importantly, the Mn_3O_4 Nfs had both SOD- and CAT-like activities, enabling a cascade ROS scavenging. First, the SOD-like activity was used for decomposing the superoxide radical ($^{\cdot}O^{2-}$) into H_2O_2, decreasing the $^{\cdot}O^{2-}$-induced damage; second, the CAT-like activity could degrade the produced H_2O_2 and provide more protection for AKI; third, due to the Nf structure, Mn_3O_4 Nfs could adsorb the released cfDNA for eliminating the immune reaction and inflammation (Scheme 1). After the intravenous (iv) administration, the Mn_3O_4 Nf treatment provided effective protection in both cisplatin-induced and IR AKI murine models in vivo. Additionally, Mn_3O_4 Nfs could perform the T_1 magnetic resonance imaging (MRI) to monitor the renal function during AKI treatment, providing a nanozyme-enabled theranostic strategy for AKI.

RESULTS AND DISCUSSION

Synthesis, ROS-Scavenging Activity, and cfDNA Adsorption Capacity of Mn_3O_4 Nfs. We successfully obtained the monodispersed Mn_3O_4 Nfs through the reported strategy.[48,49] A transmission electron microscopy (TEM) image showed the flower-like morphology of Mn_3O_4 Nfs, and their size was about 110 ± 8 nm (Figure 1a). DLS (dynamic light scattering) showed a low polymer dispersity index (PDI) (PDI = 0.283), demonstrating good dispersity (Figure 1b). It also revealed the negative charges of Mn_3O_4 Nfs (Figure S1). It is known that the surface oxidation state plays a key role in the enzyme-like activities of metal oxides. Therefore, X-ray photoelectron spectroscopy (XPS) was performed to probe the surface chemistry of Mn_3O_4. The peaks of Mn $2p_{3/2}$ and $2p_{1/2}$ were at 641.5 and 653.1 eV, respectively (Figure S2), which was consistent with a previous report.[50] The total ratio of Mn^{2+}:Mn^{3+}:Mn^{4+} was about 1:3:2, and such a valency distribution would endow Mn_3O_4 Nfs with the dual enzyme-like activities (vide infra).

We and others reported the SOD-like activity of manganese oxides (such as Mn_3O_4 and MnO_2),[49−52] which could dismutate $^{\cdot}O^{2-}$ into low-toxic H_2O_2, one type of strong ROS involved in AKI. Therefore, we first investigated the SOD-like activity of Mn_3O_4 Nfs by using a specific probe dihydroethidium (DHE). As shown in Figure 1c, the $^{\cdot}O^{2-}$ scavenging ability of Mn_3O_4 Nfs was concentration-dependent: 46.2% of $^{\cdot}O^{2-}$ was eliminated when the concentration was 10 μg/mL, and 56.1% of $^{\cdot}O^{2-}$ was scavenged when the concentration was 20 μg/mL. Then, we investigated their CAT-like activity since H_2O_2 is the product of SOD-like dismutation and is another ROS that would also cause the cellular injury. The CAT-like activity of Mn_3O_4 Nfs was measured by using a dissolvent oxygen electrode. As shown in Figure 1d, the decomposing H_2O_2 ability of Mn_3O_4 Nfs was also in a concentration-dependent manner. Moreover, a higher concentration led to a higher oxygen generation, demonstrating the CAT-like activity of Mn_3O_4 Nfs. Previously, we reported the 7−8 nm Mn_3O_4 nanoparticles (designated as small Mn_3O_4 Nps) for ROS scavenging, which exhibited satisfactory protection against ear inflammation and inflammatory bowel disease (IBD).[50,51] Here, we performed a comparison study between the small Mn_3O_4 Nps and Mn_3O_4 Nfs. As shown in Figure S3, the Mn_3O_4 Nfs showed higher CAT-like but lower SOD-like activities than the small Mn_3O_4 Nps. Similarly, by combining the dual enzyme-mimicking activities together and forming a cascade reaction for ROS scavenging, we expected that the Mn_3O_4 Nfs would be effective for AKI therapy.

In addition to ROS, cfDNAs are also involved in AKI,[53] which aggregates the AKI through the inflammatory cascade.[54] Considering that Mn_3O_4 Nfs had large specific surface areas, which would endow the Mn_3O_4 Nfs with cfDNA-adsorbing capacity, we measured the specific surface area of Mn_3O_4 Nfs and explored their cfDNA adsorbing capacity. BET (Brunauer−Emmett−Teller) measurements showed that the specific surface area of Mn_3O_4 was up to 90.2524 m^2/g. Next, we explored the cfDNA-adsorbing ability of Mn_3O_4 Nfs by incubating cfDNA with the Nfs. Fluorescence-quenching analysis demonstrated that Mn_3O_4 Nfs could efficiently quench the fluorescence by adsorbing the cfDNA (Figure 1e); gel electrophoresis also demonstrated that Mn_3O_4 Nfs had a high cfDNA-adsorbing ability (Figure S5). Moreover, the cfDNA-adsorbing ability of mesoporous silicon nanoparticles (MSNs), which had a similar structure, was evaluated. We found that MSNs had no cfDNA-adsorbing ability (Figure S6). We regarded that the mechanism of Mn_3O_4 Nfs absorbing cfDNA was due to the structures and chemical properties of both Nfs and DNA, which was also consistent with the fluorescent quench after co-incubation, as shown in Figure 1e. The above results indicated that the Mn_3O_4 Nfs could be used for the cfDNA adsorption and consequently for improving AKI therapy.

Now that the dual enzyme-mimicking activities and cfDNA adsorption ability were identified, we explored the stability of Mn_3O_4 Nfs in vitro by incubating them with different solvents. Different size changes were observed among solvents (Figure S7a). After incubation with PBS for 72 h, no intact Mn_3O_4 Nfs were observed (Figure S7b−d). The degradation of Mn_3O_4 Nfs in PBS was attributed to the reaction between phosphate saline and Mn_3O_4 Nfs, which exhibited good biocompatibility and would be beneficial for their applications in biomedicine. Accompanying the degradation of Mn_3O_4 Nfs, Mn^{2+} would be released from the Mn_3O_4 Nfs, which could be used for MRI. We therefore performed MRI after incubating Mn_3O_4 Nfs with PBS for 72 h. As shown in Figure 1f, there was a bright T_1 signal, and r_1 was up to 8.7782 mM^{-1} s^{-1}, suggesting promise in bioimaging.

ROS-Scavenging Activity and Anti-Apoptotic Capacity of Mn_3O_4 Nfs on a Cellular Level. Based on the ROS scavenging ability of Mn_3O_4 Nfs in vitro, we further investigated their anti-ROS ability in HK2 cells. First, we evaluated the cytotoxicity of Mn_3O_4 Nfs by the MTT assay. No significant cytotoxicity was observed at 24 h even when the concentration was up to 10 μg/mL (Figure S8a). Additionally, we explored the long-term exposure as long as 72 h and found that no obvious cytotoxicity was observed (Figure S6b). However, when incubated with PBS-degraded Mn_3O_4 Nfs, some cytotoxicity was observed at higher concentrations (Figure S8c,d). We reasoned that this was caused by released manganese ions, which could not be excreted out in a cellular culture level. Therefore, we assumed that our Mn_3O_4 Nf biocompatibility was acceptable. Then, we constructed both the H_2O_2 and LPS (induced the mixed ROS)-mediated oxidative stress models to explore the ROS scavenging activity of Mn_3O_4 Nfs. The MTT assay revealed significant protection

https://doi.org/10.1021/acsami.2c16305
ACS Appl. Mater. Interfaces 2022, 14, 50649−50663

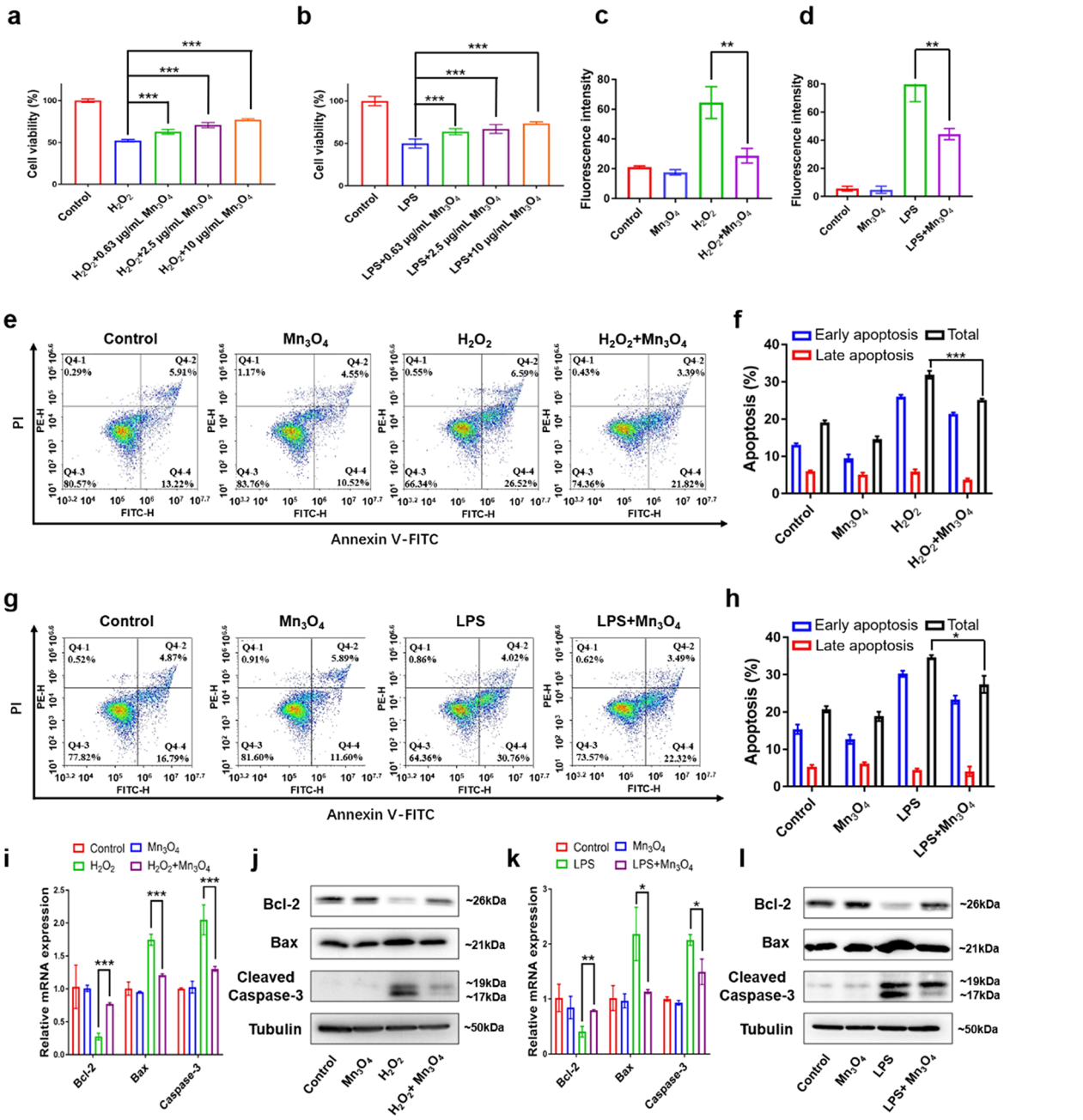

Figure 2. Antioxidative and anti-apoptotic activities of Mn_3O_4 Nfs in vitro. (a, b) Protection of Mn_3O_4 Nfs on HK2 cells against H_2O_2 (a) and LPS (b) (n = 4). (c, d) Analysis of ROS scavenging ability of Mn_3O_4 Nfs in both H_2O_2 (c) and LPS (d) models (n = 4). (e, g) Anti-apoptotic activities of Mn_3O_4 Nfs in vitro measured by flow cytometry in H_2O_2 (e) and LPS (g) models. (f, h) Quantification of apoptosis in H_2O_2 (f) and LPS (h) models (n = 3). (i, k) Relative mRNA expression of Bcl-2, Bax, and Caspase-3 in H_2O_2 (i) and LPS (k) models (n = 3). (j, l) The protein levels of Bcl-2, Bax, and cleaved-Caspase-3 in H_2O_2 (j) and LPS (l) models. (a−d, f, h, i, k) Data are shown as mean ± SD, two-tailed Student's t-test for P values (*P < 0.05, **P < 0.01, ***P < 0.001).

to HK2 in a dose-dependent manner against both the H_2O_2- and LPS-induced oxidative stress (Figure 2a,b). We also compared the cellular ROS scavenging activity of Mn_3O_4 Nfs with Mn_3O_4 Nps. As shown in Figure S9a,b, Mn_3O_4 Nps showed no obvious protection in H_2O_2-treated HK2 cells and a weaker protection than Mn_3O_4 Nfs in LPS-treated cells. We assumed that the superior cellular anti-ROS ability of Mn_3O_4 Nfs could be attributed to cascade ROS ($^{\cdot}O^{2-}$ and H_2O_2) scavenging, but the accumulation of the original and the $^{\cdot}O^{2-}$-converted H_2O_2 would cause oxidative damage in the Mn_3O_4 Np group due to its lower CAT-mimicking activity. In addition, we measured the ROS scavenging ability by confocal imaging (Figure S10a and S10b). Quantitative analysis confirmed that Mn_3O_4 Nfs possessed better ROS scavenging ability in both the H_2O_2- and LPS-induced cell models (Figure 2c,d). Additionally, $^{\bullet}OH$ is an important type of ROS, and we evaluated the $^{\bullet}OH$ scavenging ability by electron paramagnetic resonance (EPR). Mn_3O_4 Nfs exhibited $^{\bullet}OH$ scavenging ability in a concentration-dependent manner, and the trend was consistent with the $^{\bullet}O_2^-$ scavenging ability (Figure S4).

Generally, ROS can induce cell apoptosis while antioxidants can inhibit cell apoptosis by reducing oxidative stress.[55,56]

https://doi.org/10.1021/acsami.2c16305
ACS Appl. Mater. Interfaces 2022, 14, 50649−50663

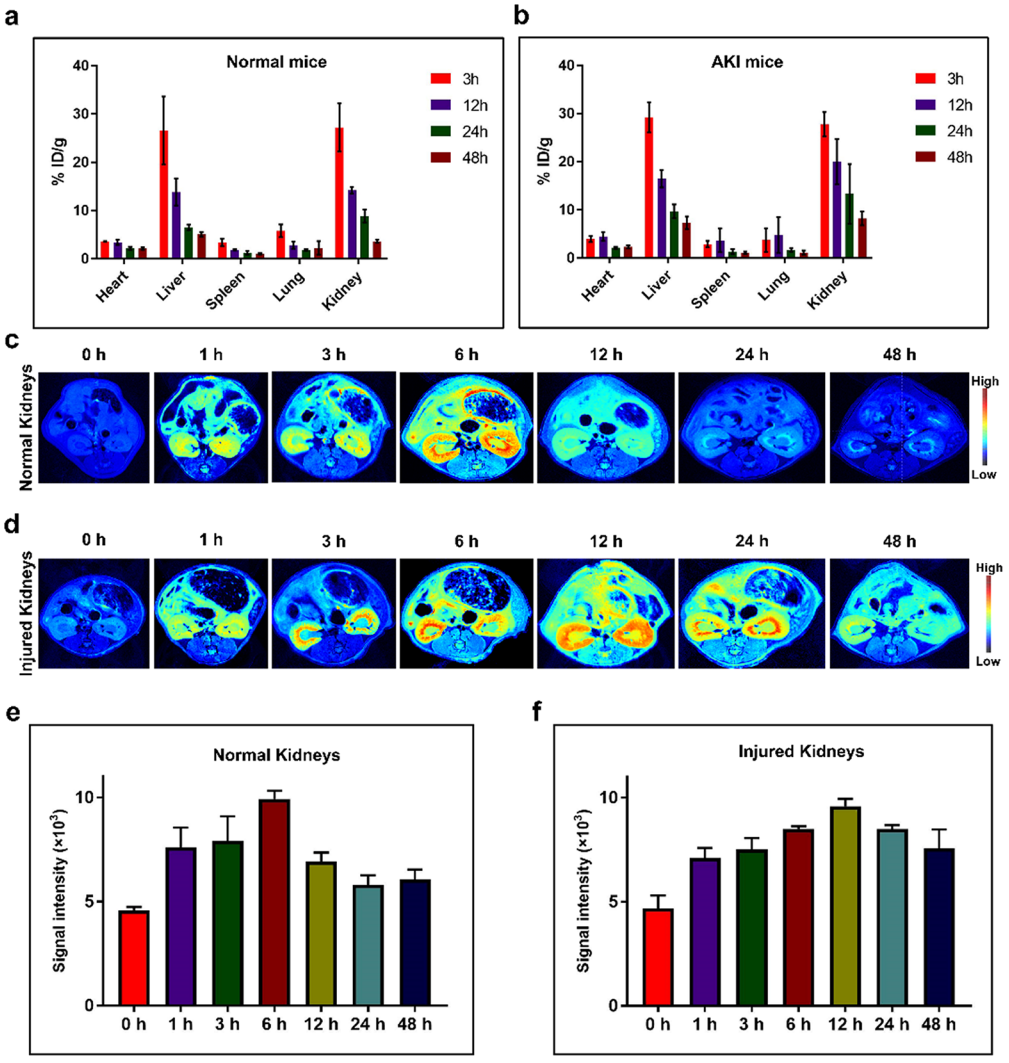

Figure 3. Biodistribution and MR imaging of Mn_3O_4 Nfs in vivo. (a) Mn content of the major organs in normal mice. (b) Mn content of the major organs in AKI mice. (c, d) Representative MR images of normal kidneys (c) and injured kidneys (d) at 9.4 T. (e, f) MRI signal intensity quantifications of normal kidneys (e) and injured kidneys (f). (a, b, e, f) Data are presented as mean ± SD (n = 3).

Hence, we investigated the anti-apoptotic ability of Mn_3O_4 Nfs in vitro. After the treatment with H_2O_2 and LPS, the amount of total apoptotic cells increased significantly. In contrast, when the cells were pretreated with Mn_3O_4 Nfs, early apoptosis showed a significant reduction in both H_2O_2 and LPS models. A significant reduction in the total amount of apoptotic cells was also observed (Figure 2e–h). Then, apoptosis-related gene expression was measured. In both H_2O_2 and LPS models, the mRNA expression levels of Bcl-2 significantly decreased and those of Bax and Caspase-3 significantly increased, which was reversed by Mn_3O_4 Nf pretreatment (Figure 2i,k). The protein levels of Bcl-2 and Bax were consistent with the mRNA expression levels (Figure 2j,l). Cleaved-Caspase-3 was the activated form of Caspase-3. Similarly, H_2O_2 and LPS treatment significantly increased the levels of cleaved-Caspase-3, which decreased after Mn_3O_4 Nf pretreatment. These results indicated that Mn_3O_4 Nfs were effective against the H_2O_2- and LPS-induced apoptosis.

Biodistribution of Mn_3O_4 Nfs In Vivo. To evaluate the biodistribution of Mn_3O_4 Nfs in vivo, normal mice and AKI mice were iv injected with Mn_3O_4 Nfs and major organs were harvested at different time points (iv 3, 12, 24, and 48 h post-injection) for inductively coupled plasma mass spectrometry (ICP-MS) analysis. The results showed that Mn_3O_4 Nfs were mainly distributed in kidneys and liver in vivo (Figure 3a,b). For normal mice, the content of Mn_3O_4 Nfs in the kidneys decreased significantly at 12 h, demonstrating the rapid clearance of Mn_3O_4 Nfs by normal renal excretion. For AKI mice, Mn_3O_4 Nfs exhibited relatively high levels of accumulation in kidneys at 12 h and significantly decreased at 24 h. Such a rapid clearance in normal mice and prolonged accumulation in injured kidneys are highly advantageous for AKI treatment.

As described above, we had confirmed the MRI function of Mn_3O_4 Nfs in vitro (Figure 1h). We reasoned that the Mn^{2+} released from Mn_3O_4 Nfs could enhance T_1-weighted MRI, and therefore, Mn_3O_4 Nfs could be used as contrast agents to evaluate renal function in vivo. Forty milligrams per kilogram of cisplatin was used to establish the cisplatin-induced AKI model by intraperitoneal injection. After 24 h of injection, "0 h" T_1-weighted MRI was performed on both AKI mice and healthy mice. Then, both groups of mice were iv injected with Mn_3O_4 Nfs, time-point MR imaging was performed, and changes in major organs were observed dynamically. In the

https://doi.org/10.1021/acsami.2c16305
ACS Appl. Mater. Interfaces 2022, 14, 50649−50663

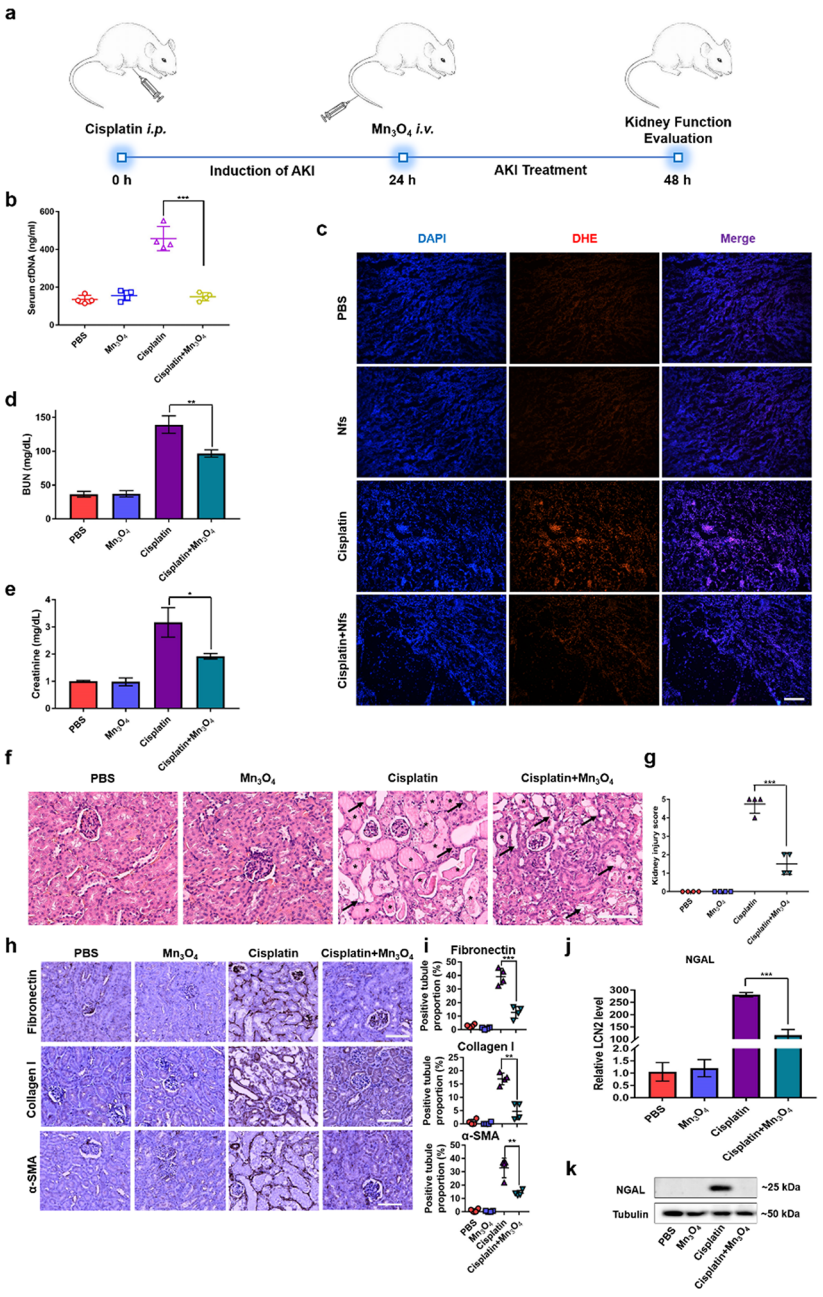

Figure 4. Assessment of ROS- and cfDNA-scavenging activities in vivo and protective effect on renal function with Mn_3O_4 Nf intravenous injection for the cisplatin-induced AKI mouse model. (a) Schematic illustration of the establishment of a cisplatin-induced AKI mouse model and Mn_3O_4 Nf treatment. (b) cfDNA-scavenging activities of Mn_3O_4 Nfs in vivo (n = 4). (c) DHE staining results of kidneys. Scale bar: 200 μm. (d) Blood urea nitrogen (BUN) measurement (n = 4). (e) Serum creatinine measurement (n = 4). (f) H&E staining results of kidneys. Injured renal tubules are marked with arrows, and the formed casts are marked with asterisks. Scale bar: 100 μm. (g) Kidney injury score assessment (n = 4). (h) Immunohistochemical staining of fibronectin, collagen I, and α-smooth muscle actin (α-SMA) in kidney sections. Scale bar: 100 μm. (i) Quantitative results of positive tubule proportion with fibronectin, collagen I, and α-SMA staining (n = 4). (j) The mRNA levels of neutrophil gelatinase-associated lipocalin (NGAL) in renal tissues (n = 4). (k) The protein levels of NGAL in renal tissues measured by Western blot. (b–e, g, i, j) Data are shown as mean ± SD, two-tailed Student's t-test for P values (*P < 0.05, **P < 0.01, ***P < 0.001).

control group, the brightest MRI signal was obtained at 6 h after injection (Figure 3c,e) and was decreased after 12 h due to the Mn_3O_4 Nfs' degradation and renal excretion. However, in AKI mice, the brightest signal was obtained at 12 h, and the MRI signal was still observed after 48 h (Figure 3d,f). We assumed that this was due to the Mn_3O_4 Nfs' large amount of uptake and/or delayed excretion by the impaired-renal tubular cells in the AKI model. Moreover, the prolonged MRI signal reflected impaired renal excretory function induced by cisplatin. These results revealed that Mn_3O_4 Nfs could be used as an assessment probe of renal function via MRI.

Therapeutic Efficacy of Mn_3O_4 Nfs in a Cisplatin-Induced AKI Model In Vivo. In view of the superior cfDNA-scavenging ability and the cascade ROS-scavenging capacity in vitro, Mn_3O_4 Nfs should be effective in AKI treatment. Typically, 20 to 40% of patients develop AKI as a serious adverse event when they are exposed to cisplatin.[57] ROS overproduction is the main cause of cisplatin nephrotoxicity.[58]

https://doi.org/10.1021/acsami.2c16305
ACS Appl. Mater. Interfaces 2022, 14, 50649−50663

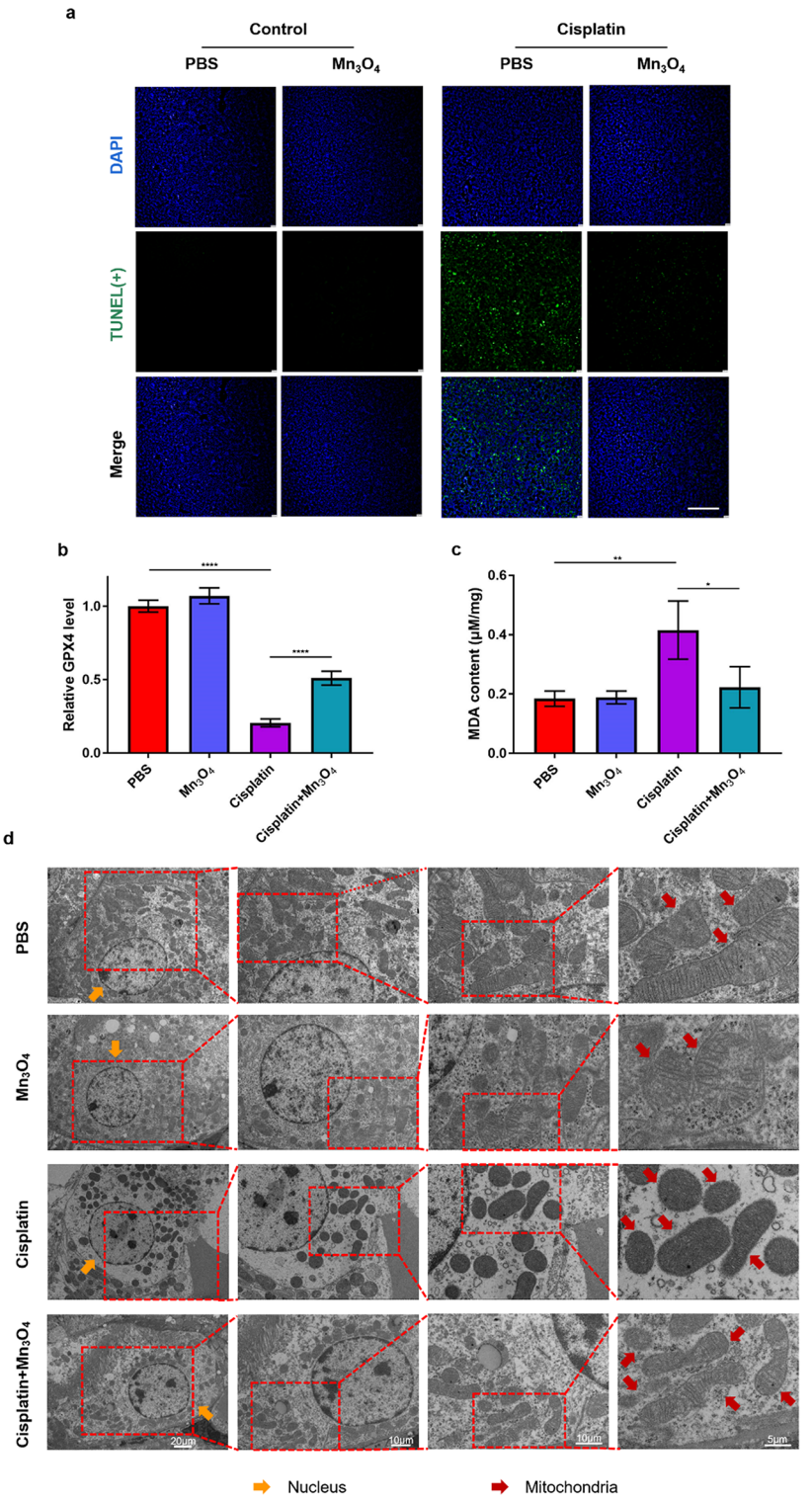

Figure 5. Evaluation of anti-apoptosis and anti-ferroptosis activities of Mn_3O_4 Nfs for treating cisplatin-induced AKI. (a) TUNEL staining in frozen kidney sections. Scale bar: 150 μm. (b) The mRNA expression levels of GPX4 in renal tissues (n = 4). (c) Assessment of MDA levels in renal tissues (n = 4). (d) TEM images of renal tissues in different treatment groups. Orange arrows, nucleus; red arrows, mitochondria. Scale bars: from left to right are 20, 10, 10, and 5 μm, respectively. (b, c) Data are shown as mean ± SD, two-tailed Student's t-test for P values (*P < 0.05, **P < 0.01, ***P < 0.001).

In addition, it is suggested that the levels of mtDNA in the plasma of patients receiving platinum-based chemotherapy were higher than those of healthy controls, which could exacerbate cisplatin-induced AKI.[38] Therefore, cfDNA may be one of the reasons for cisplatin-induced AKI. The cisplatin-induced AKI mouse model was constructed and used to explore the protective effect of Mn_3O_4 Nfs. As illustrated in Figure 4a, mice were intraperitoneally injected with cisplatin to construct the AKI model (PBS-treated as the control group). After 24 h, Mn_3O_4 Nfs were iv injected to both PBS- and

https://doi.org/10.1021/acsami.2c16305
ACS Appl. Mater. Interfaces 2022, 14, 50649−50663

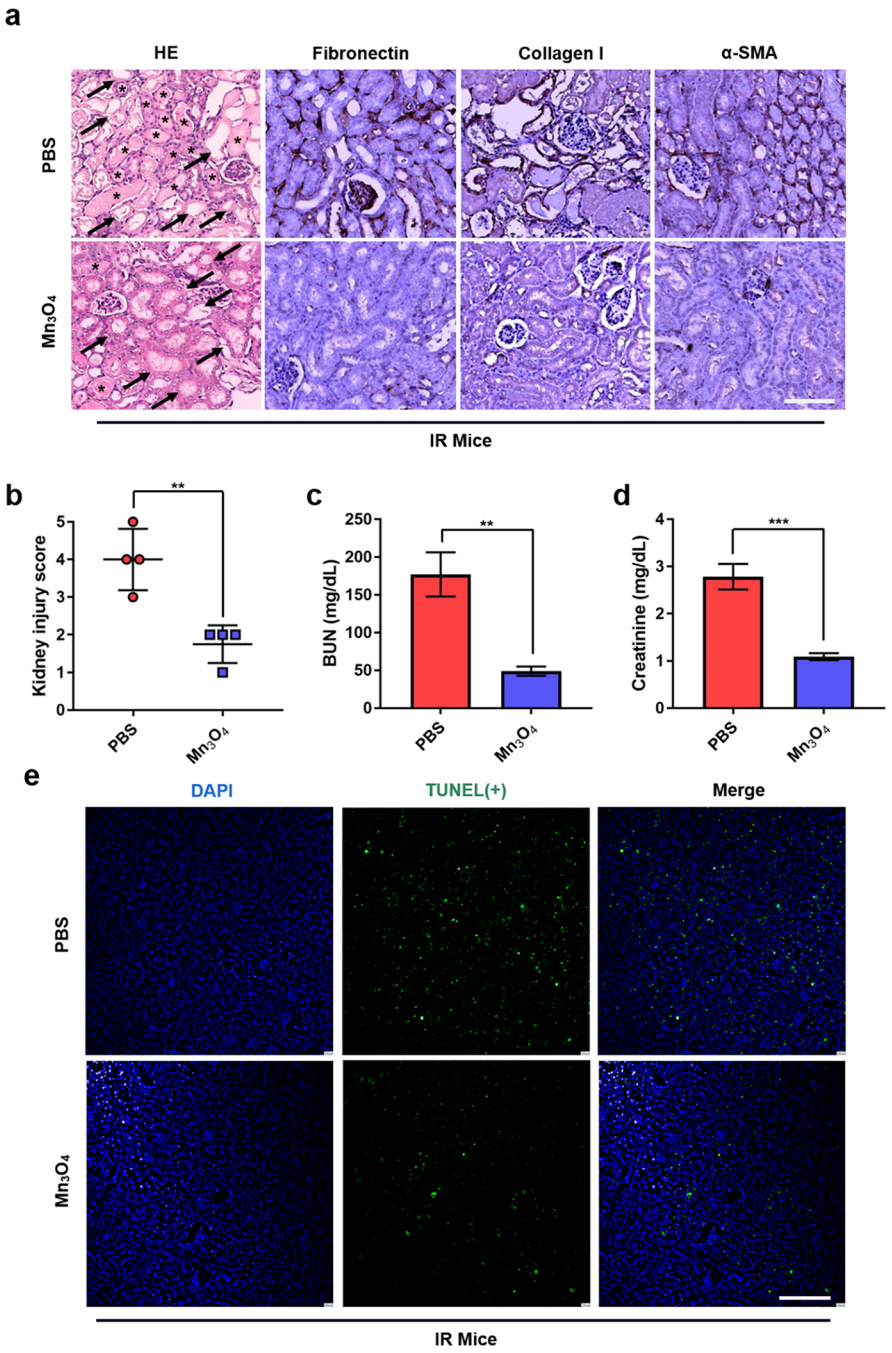

Figure 6. Assessment of therapeutic efficacy with Mn_3O_4 Nf intravenous injection for the IR-AKI mouse model. (a) H&E and IHC (fibronectin, collagen I, and α-SMA) staining results of kidneys. Injured renal tubules are marked with arrows, and the formed casts are marked with asterisks. Scale bar: 100 μm. (b) Kidney injury score assessment (n = 4). (c) Blood urea nitrogen (BUN) measurement (n = 4). (d) Serum creatinine measurement (n = 4). (e) TUNEL staining in frozen kidney sections. Scale bar: 150 μm. (b–d) Data are shown as mean ± SD, two-tailed Student's t-test for P values (**P < 0.01, ***P < 0.001).

cisplatin-treated mice. Both the blood samples and renal tissues were harvested at 48 h to assess the protective effect of Mn_3O_4 Nfs. As shown in Figure 3b, Mn_3O_4 Nfs could reduce the amount of serum cfDNAs in cisplatin-induced AKI mice in vivo (Figure 4b), demonstrating that Mn_3O_4 Nfs decreased the level of serum cfDNA by adsorption. Furthermore, we found that the level of cfDNA in urine increased after Mn_3O_4 Nf treatment in AKI mice (Figure S11). We considered that cfDNA in serum was adsorbed by Mn_3O_4 Nfs and was then removed by kidneys into urine. cfDNA triggered the inflammatory response and may lead to tissue damage. A major concern was that whether cfDNA carried by Mn_3O_4 Nfs caused damage to major organs, especially kidneys. Mn_3O_4 Nfs and cfDNA were co-incubated to form Mn_3O_4 Nfs-cfDNA, which was injected iv into mice. No renal tissue damage or liver/kidney function impairment was observed after Mn_3O_4 Nf–cfDNA injection (Figure S12a–f), suggesting that cfDNA carried by Mn_3O_4 Nfs may not cause extra damage. Except for the cfDNA decrease, $^{\cdot}O^{2-}$ was efficiently eliminated in the Mn_3O_4 Nf group in cisplatin-induced AKI mice by detecting $^{\cdot}O^{2-}$ in frozen kidney sections (Figure 4c). Both cfDNA and

https://doi.org/10.1021/acsami.2c16305
ACS Appl. Mater. Interfaces 2022, 14, 50649–50663

ROS scavenging capacities were consistent with the above in vitro results and demonstrated the protection against AKI.

Apart from the cfDNA and ROS scavenging, the levels of blood urea nitrogen (BUN) and serum creatinine were used to evaluate renal function. Mn_3O_4 Nf treatment decreased the levels of these two factors, demonstrating the impair-repairing function (Figure 4d,e). H&E staining was used to estimate kidney-related damage, including cast formation, tubular necrosis, loss of brush border, and dilatation of tubules. Cisplatin plus Mn_3O_4 Nf treatment showed the attenuation of tubular damage (Figure 4f,g). Renal fibrosis is the end stage of all kidney diseases,[59,60] which could occur after severe AKI and eventually lead to chronic kidney diseases.[61−63] Hence, fibrosis-related markers, including fibronectin, collagen I, and α-smooth muscle actin (α-SMA), were evaluated by IHC staining. The same results were obtained: cisplatin plus Mn_3O_4 Nf treatment attenuated all these markers (Figure 4h,i). Moreover, neutrophil gelatinase-associated lipocalin (NGAL, also known as LCN2) is another important AKI biomarker that is closely associated with kidney injury.[64,65] Mn_3O_4 Nf treatment significantly decreased both the mRNA and protein expression levels of NGAL (Figure 4j,k). Kidney injury molecule-1 (KIM-1, also known as HAVRC1) and heme oxygenase-1 (HO-1, also known as HMOX1) are two critical AKI biomarkers that play a role in the pathological process of AKI and reflect the degree of kidney injury.[66,67] Mn_3O_4 Nf treatment also significantly decreased their mRNA levels (Figures S13 and S14). These results indicated that Mn_3O_4 Nf treatment could significantly restore the expression of these factors in the AKI model.

Combined, the above results indicate that Mn_3O_4 Nf treatment was able to remove serum cfDNAs and eliminate excessive ROS, promoted the recovery of renal function and kidney-related damage, and decreased the expression of the fibrosis-related markers in the cisplatin-induced AKI model.

Anti-Apoptosis and Anti-Ferroptosis Capacities of Mn_3O_4 Nfs in AKI Therapy. To better understand the therapeutic mechanism of Mn_3O_4 Nfs toward AKI, the anti-apoptosis and anti-ferroptosis capacities were investigated. First, as shown in Figure 5a, TUNEL staining indicated that Mn_3O_4 Nfs significantly diminished the apoptosis induced by cisplatin. Apart from apoptosis, ferroptosis is characterized by excessive lipid peroxidation[68] and is also involved in cisplatin-induced AKI.[69] Therefore, we investigated the anti-ferroptosis capacity of the Mn_3O_4 Nfs. GPX4 (glutathione peroxidase 4), a major antioxidant enzyme against ferroptosis,[70] showed higher expression in cisplatin plus Mn_3O_4 Nf treatment (Figure 5b); MDA (malondialdehyde), one of the main products of lipid peroxidation,[71] was significantly decreased with the Mn_3O_4 Nf treatment (Figure 5c). Furthermore, bio-TEM imaging of the renal cortex revealed that cisplatin-treated mice showed shrunken mitochondria, the major morphological characteristic of ferroptosis.[70] Mitochondrial morphology significantly improved in Mn_3O_4 Nf-treated mice (Figure 5d). The ATP levels were measured to evaluate the mitochondrial function. Cisplatin led to a decrease in ATP levels, which was reversed by Mn_3O_4 Nf treatment, indicating improvement in mitochondrial function (Figure S15). These results indicated that the Mn_3O_4 Nfs could protect cells against ferroptosis by regulating the expression of key factors and recovering the mitochondrial morphology.

Therapeutic Efficacy of Mn_3O_4 Nfs in the IR-AKI Model In Vivo. In addition to the cisplatin exposure, IR is another major cause of AKI.[72] The accumulation of ROS during IR promotes IR-AKI.[73] One study revealed that plasma cf-mtDNA levels increased after IR injury, which may aggravate the inflammatory response and tissue damage of IR-AKI.[39] Therefore, we subsequently investigated the therapeutic efficacy of Mn_3O_4 Nfs in IR-induced AKI mice. The IR model was established by unilateral renal pedicle clamping for 45 min (ischemia) and subsequently disentangling (reperfusion), as described previously.[74,75] Then, Mn_3O_4 Nfs were iv injected and kidneys were harvested at 24 h to measure the histological changes. First, Mn_3O_4 Nfs reduced the expression of fibrosis-related markers, including fibronectin, collagen I, and α-SMA (Figure 6a). Second, the kidney injury score was decreased with Mn_3O_4 Nf treatment (Figure 6b). Last, the contralateral kidney was resected during the surgery and blood samples were used for BUN and serum creatinine detection. The Mn_3O_4 Nf treatment significantly decreased the levels of BUN and serum creatinine (Figure 6c,d). TUNEL staining showed that Mn_3O_4 Nf treatment significantly reduced the apoptosis of renal tissues in IR models (Figure 6e). The expressions of AKI biomarkers (KIM-1, HO-1, and NGAL) also significantly decreased after Mn_3O_4 Nf treatment (Figure S16). All these results demonstrated that Mn_3O_4 Nfs could improve renal function and show excellent therapeutic efficacy on IR-induced AKI mice as well as the cisplatin-induced AKI model.

Biocompatibility Assessment. To evaluate the biocompatibility of Mn_3O_4 Nfs, we set a series of doses (5, 10, and 20 mg/kg) and measured the liver/kidney function and inflammatory response after treatment. In addition to normal mice, the biocompatibility of Mn_3O_4 Nfs in AKI mice was also evaluated, since AKI mice were more likely to be susceptible to harmful stimulation. The results showed that each dose of Mn_3O_4 Nfs caused no damage to liver/kidney function (Figure S17a−d) and no increase in inflammatory cytokine levels (Figure S17e−g) in normal mice. Cisplatin induced damage to liver/kidney function and raised the levels of inflammatory cytokines. Mn_3O_4 Nf treatment did not lead to extra damage. In contrast, it improved liver/kidney function and decreased the levels of inflammatory cytokines in serum, indicating a remarkable therapeutic effect.

We further evaluated the biosafety of Mn_3O_4 Nfs to major organs by histological methods. The iv injection of Mn_3O_4 Nfs (10 mg/kg) was performed on healthy mice. Then, major organs, including heart, liver, spleen, lungs, and kidneys, were harvested after 24 h and 1 month for short-term and long-term toxicity measurements, respectively. With Mn_3O_4 Nf treatment, there was no obvious damage by H&E staining of major organs at 24 h and 1 month (Figures S18 and S19), demonstrating its satisfactory compatibility in vivo. The good biocompatibility of Mn_3O_4 Nfs would facilitate their future bio-transformation in AKI treatment.

CONCLUSIONS

In conclusion, smart Nf-structured Mn_3O_4 Nfs were developed for AKI protection through a cascade ROS scavenging and cfDNA adsorption. On the one hand, due to the dual enzyme-mimicking activities, a cascade ROS scavenging was demonstrated by dismutating $^{\cdot}O^{2-}$ into H_2O_2 and then decomposing it into H_2O; on the other hand, due to the high specific surface area, effective cfDNA adsorption was achieved. Combining ROS scavenging and cfDNA adsorption, Mn_3O_4 Nfs showed a promising application in AKI. In vivo studies showed that

https://doi.org/10.1021/acsami.2c16305
ACS Appl. Mater. Interfaces 2022, 14, 50649−50663

Mn_3O_4 Nfs were efficient to eliminate cfDNAs and were effective against kidney injury induced by both cisplatin and IR, demonstrating satisfactory therapeutic efficacy for AKI in a mouse model. In addition, Mn_3O_4 Nfs could be used as an MRI contrast agent and its signal could also be used to assess the real-time renal function. Therefore, Mn_3O_4 nanozymes, as a rational therapeutic material, provided a potential treatment option for clinical AKI.

MATERIALS AND METHODS

Chemicals. Potassium permanganate ($KMnO_4$), H_2O_2, and oleic acid were obtained from Sinopharm Chemical Reagent Co., Ltd. (Shanghai, China). DHE, free DNA from the calf thymus, and lipopolysaccharide (LPS) were purchased from Sigma Co., Ltd. (Shanghai, China). Human renal tubular epithelial cells (HK2 cells) were purchased from the Cell Bank of Shanghai Institutes for Biological Sciences (Shanghai, China). Fetal bovine serum was purchased from Wisent (Nanjing, China). Penicillin−streptomycin were from Gibco (Massachusetts, USA). Dichlorofluorescin diacetate (DCFH-DA), 4′,6-diamidino-2-phenylindole (DAPI), Lipid Peroxidation MDA Assay Kit, and ATP Assay Kit were purchased from Beyotime Biotech (Shanghai, China). Annexin V-FITC/PI Apoptosis Detection Kit, TUNEL BrightGreen Apoptosis Detection Kit, and AceQ qPCR SYBR Green Master Mix were purchased from Vazyme Biotech (Nanjing, China). Diaminobenzidine (DAB) was from ZSGB-BIO (Beijing, China). Optimum cutting temperature (OCT) gel was from Sakura Finetek (Torrance, USA). TRIzol reagent was from Invitrogen Biotech (Carlsbad, USA). The PrimeScript RT Reagent Kit was purchased from Takara (Otsu, Japan). The antibodies used for IHC were as follows: fibronectin (Abcam, Cambridge, UK, Catalog No. ab2413, 1:400), collagen I (Abcam, Catalog No. ab34710, 1:400), and α-SMA (Abcam, Catalog No. ab5694, 1:3000). The antibodies used for Western blotting were as follows: Bcl-2 (Abcam, Catalog No. ab32124, 1:1000), Bax (Proteintech, Wuhan, China, Catalog No. 50599-2-Ig, 1:1000), Cleaved-Caspase-3 (CST, Massachusetts, USA, Catalog No. #9662, 1:1000), and NGAL (Vazyme Biotech, Nanjing, China, 1:4000). Quant-iT PicoGreen dsDNA reagent was from Thermo Fisher Scientific (Shanghai, China). DNeasy Blood & Tissue Kit was from QIAGEN (Germany). The QuantiChrom Urea Assay Kit and the QuantiChrom Creatinine Assay Kit were purchased from Bioassay Systems (Hayward, California, USA). The Alanine Aminotransferase (ALT/GPT) Activity Assay Kit and the Aspartate Aminotransferase (AST/GOT) Activity Assay Kit were purchased from Elabscience Biotechnology Co., Ltd. (Wuhan, China). The Mouse IL-6 ELISA Kit, the Mouse IL-1β ELISA Kit, and the Mouse TNF-α ELISA Kit were purchased from Fcmacs Biotech Co., Ltd. (Nanjing, China).

Synthesis and Characterization of Mn_3O_4 Nfs. Mn_3O_4 Nfs were synthesized according to a previous report.[48,50] Briefly, 1 g of $KMnO_4$ was dissolved in 500 mL of H_2O and violently stirred for 30 min; then, 10 mL of oleic acid was added and stirred for another 5 h at 28 °C to obtain the precursor. The precursor was dried at 80 °C for 10 h and then calcined in air at 200 °C for 5 h to obtain the product.

The size and zeta potential of the Mn_3O_4 Nfs were obtained by using a transmission electron microscope (TEM) and DLS. Power X-ray diffraction (XRD) and XPS were also used to identify the structure of Mn_3O_4 Nfs. The ROS-scavenging ability was measured by the DHE probe. The biostability of Mn_3O_4 was detected by incubating Mn_3O_4 with different solvents, such as water, phosphate buffer (PBS), and culture medium, and morphology and size changes were obtained by TEM and DLS. MRI was carried out by incubating Mn_3O_4 with PBS, and the released Mn^{2+} was used for MRI.

In Vitro Cytotoxicity of Mn_3O_4 Nfs. HK2 cells were cultured in Dulbecco's modified Eagle's medium (DMEM) containing 10% fetal bovine serum and 1% penicillin−streptomycin under a water-saturated atmosphere of 5% CO_2 at 37 °C. To evaluate the cytotoxicity of Mn_3O_4 Nfs, HK2 cells were seeded in 96-well plates with a density of 5×10^3 cells per well and cultured for 24 h. Then, the cells were treated with Mn_3O_4 Nfs with different concentrations (0.16, 0.32, 0.63, 1.25, 2.5, 5, and 10 μg/mL) for another 24 or 72 h. Cell viability was evaluated by the MTT assay.

In Vitro Protective Effect of Mn_3O_4 Nfs on HK2 Cells against H_2O_2 and LPS. HK2 cells were sub-cultured into 96-well plates with a density of 5×10^3 cells per well for 24 h; next, cells were treated with Mn_3O_4 Nfs or Mn_3O_4 NPs in different concentrations for 6 h and washed with PBS; later, cells were co-incubated with H_2O_2 (900 μM) or LPS (100 μg/mL) for 24 h; and finally, the protective effect was evaluated by cell viability.

Intracellular ROS Scavenging Detection. A fluorogenic probe, DCFH-DA, was used to measure the intracellular level of ROS. HK2 cells with a density of 5×10^5 cells per well were sub-cultured in six-well plates. Then, the cells were pretreated with Mn_3O_4 Nfs for 6 h and incubated with H_2O_2 or LPS for another 12 h. The culture medium was removed and washed with PBS three times. DCFH-DA (0.01 mM) in FBS-free DMEM was added to each well for culturing for 30 min. Then, the medium was refreshed three times, and fluorescence was observed under a fluorescence microscope (EVOS FL Auto 2, Thermo Fisher Scientific, Waltham, Massachusetts, USA) with the excitation and emission wavelengths at 488 and 525 nm, respectively. The fluorescence intensity was quantified with ImageJ v1.8.0.

In Vitro Anti-Apoptotic Activity of Mn_3O_4 Nfs. HK2 cells with a density of 5×10^5 cells per well were seeded in six-well plates for 24 h. Then, the cells were pretreated with Mn_3O_4 Nfs for 6 h and incubated with H_2O_2 or LPS for another 12 h. The anti-apoptotic activity of Mn_3O_4 Nfs in vitro was monitored by using the Annexin V-FITC/PI Apoptosis Detection Kit. The test was performed following the protocol provided by the manufacturers. The percentage of apoptotic cells was detected by a Beckman CytoFLEX flow cytometer.

Cisplatin-Induced and IR AKI Mouse Models. The protocols of all animal experiments were approved by the Institutional Animal Care and Use Committee, Nanjing Drum Tower Hospital, Affiliated Medical School of Nanjing University. To establish the cisplatin-induced AKI model, male ICR mice (6−7 weeks) were intraperitoneally injected with cisplatin (40 mg/kg). For the IR-AKI mouse model, mice were anesthetized with isoflurane inhalation and injected with buprenorphine subcutaneously for analgesia. As described earlier,[76] the IR-AKI mouse model was established by unilateral renal pedicle clamping for 45 min (ischemia) and subsequent disentangling (reperfusion). In brief, after removing the left renal hilus fat and isolating the renal vessels completely, the mice were placed on a 38 °C heating plate, and the renal pedicle was entirely clamped with vascular bulldog clamps for 45 min. Subsequently, the bulldog clamp was released slowly, and the sign of successful reperfusion was that the color of the left kidney changed from purple-black to red. In the sham group, the left renal pedicle of the mice was only isolated but not clamped.

To evaluate the therapeutic efficacy of Mn_3O_4 Nfs in vivo, for the cisplatin-induced AKI model, the mice were divided into four groups: PBS, Mn_3O_4, cisplatin, and cisplatin+Mn_3O_4. For the IR-AKI model, the mice were divided into two groups: IR and IR + Mn_3O_4. Twenty-four hours after intraperitoneal injection of cisplatin or PBS and immediately after the IR model was established, both AKI mice and healthy mice were iv injected with Mn_3O_4 Nfs (10 mg/kg).

ICP-MS Analysis. For ICP-MS analysis, the healthy and cisplatin-induced AKI mice (n = 3) were injected iv with Mn_3O_4 Nfs (10 mg/kg, 100 μL). Then, the mice were sacrificed to harvest major organs (heart, liver, spleen, lung, kidney) at different time points (3, 12, 24, and 48 h). The organs were digested with aqua regia, and ICP-MS was performed to detect the amount of Mn in the major organs. The percent of injected dose per gram of tissues of Mn was calculated.

H&E and IHC Staining of Kidney Sections. Mice were sacrificed, and renal tissues were harvested at 48 h in the cisplatin-induced AKI model and at 24 h in the IR-AKI model. The collected renal tissues were fixed with paraformaldehyde (4% in PBS), embedded in paraffin, and then sectioned at 5 μm. The sections were first used for H&E staining. The staining results were analyzed to evaluate and score the degree of kidney injury. The final score reflected the degree of cast formation, tubular necrosis, loss of brush

https://doi.org/10.1021/acsami.2c16305
ACS Appl. Mater. Interfaces 2022, 14, 50649−50663

Table 1. Primer Sequences

gene name	forward primer	reverse primer
ACTB	GGCTGTATTCCCCTCCATCG	CCAGTTGGTAACAATGCCATGT
Bcl-2	GACTGAGTACCTGAACCGGCATC	CTGAGCAGCGTCTTCAGAGACA
BAX	CAGTTGAAGTTGCCATCAGC	CAGTTGAAGTTACCATCAGC
Caspase-3	CATGGAAGCGAATCAATGGACT	CTGTACCAGACCGAGATGTCA
Havcr1	ACATATCGTGGAATCACAACGAC	ACAAGCAGAAGATGGGCATTG
Hmox1	AGGTACACATCCAAGCCGAGA	CATCACCAGCTTAAAGCCTTCT
Lcn2	TGGCCCTGAGTGTCATGTG	CTCTTGTAGCTCATAGATGGTGC
GPX4	TGTGCATCCCGCGATGATT	CCCTGTACTTATCCAGGCAGA

border, and tubular dilation in 10 randomly selected, non-overlapping fields (200×) as follows: 0, none; 1, ≤10%; 2, 11% to 25%; 3, 26% to 45%; 4, 46% to 75%; and 5, ≥76%.

Renal sections were also used for immunohistochemistry (IHC) staining to detect the expression of extracellular matrix proteins, including fibronectin, collagen I, and α-SMA. IHC staining was performed following standard protocols of Cell Signaling Technology. DAB was used as a horseradish peroxidase-specific substrate. Photographs of representative fields were captured under a high-power magnification microscope (×200) via Leica LAS v4.12 software. The positive tubule proportion of each image was counted and analyzed with Image-Pro Plus v6.0.

In Vivo ROS-Scavenging Activity of Mn_3O_4 Nfs. Partial renal tissues were stored in OCT gel at −20 °C to make frozen sections (5 μm). To detect superoxide radical production in vivo, the frozen renal sections were prepared and incubated with 0.3% Triton X-100 for 15 min at room temperature. Then, the solution was removed, and subsequently, the sections were stained with DHE (1 mM) for 30 min. Then, the sections were washed with PBS three times and incubated with DAPI. Fluorescence was observed under a fluorescence microscope. The frozen renal sections were also used to measure the anti-apoptotic activity of Mn_3O_4 Nfs in vivo with the TUNEL method. After fixation with 4% PFA for 30 min and incubation with 0.2% Triton X-100 for 15 min, the sections were stained with a TUNEL BrightGreen Apoptosis Detection Kit. The test was performed following the protocol provided by the manufacturers. Fluorescence was observed under a fluorescence microscope.

TEM Analysis of Renal Tissue. Partial renal tissues were used in TEM analyses. First, the renal cortex was sectioned and divided into tissue masses of 1 mm^2. Then, the tissue mass was fixed at 4 °C for 24 h. The fixed tissues were rinsed three times with PBS for 20 min each time, centrifuging and discarding the supernatant after each rinse. Precooled 1% osmic acid was then used to fix the tissues at 4 °C for 2−3 h. The tissues were rinsed with PBS 3 times for 20 min each time. The tissues were dehydrated by immersing them in a series of gradient alcohol (30, 50, 70, 80, 85, 90, 95, and 100%), each concentration of alcohol for 15 min. Then, the tissues were dehydrated again with 100% alcohol twice, each for 10 min. Penetration was then carried out with osmotic agents, which were acetone:epoxy resin (2:1), acetone:epoxy resin (1:1), and epoxy resin in turn. The penetration process occurred at 37 °C for 12 h each time. The treated tissues were put into a small capsule, and the embedding agent epoxy resin was added. After setting at 60 °C for 48 h, the samples were trimmed to a suitable size and sliced with a slicer (60−100 nm). The sections can be observed under an electron microscope after double staining with plumbum and uranium.

Quantitative Real-Time PCR (qRT-PCR). To measure the mRNA expression levels of AKI markers and GPX4, total RNA of partial renal tissues was extracted with TRIzol reagent. Reverse transcription was performed with the PrimeScript RT Reagent Kit for cDNA synthesis. AceQ qPCR SYBR Green Master Mix was used to perform PCR, and the reactions were run on a StepOnePlus (Applied Biosystems, Foster City, USA). The relative mRNA expression level was normalized to that of ACTB by using the $2^{-\triangle\triangle CT}$ method. The primer sequences are shown in Table 1.

Western Blot. To detect the expression of NGAL, the extracted proteins from partial renal tissues were subjected to Western blot analysis as previously described.[77]

MDA Detection. To detect the MDA levels of renal tissues, the proteins were extracted from mouse kidneys. The MDA levels were evaluated by using the Lipid Peroxidation MDA Assay Kit. The test was performed following the protocol provided by the manufacturers.

ATP Level Detection. To detect the ATP levels, renal tissues were homogenized, and the supernatant was extracted. The ATP levels were measured by using the ATP Assay Kit. The test was performed following the protocol provided by the manufacturers.

cfDNA Scavenging Assay. First, we tested the DNA-adsorbing ability of Mn_3O_4 Nfs in vitro. In brief, 25 μL of free DNA from the calf thymus (10 μg/mL) and 25 μL of PicoGreen were mixed in a 96-well plate. Then, 50 μL of water was added to each well, and the plate was shaken for 30 min in the dark to form the DNA−dye complex. Subsequently, 100 μL of Mn_3O_4 Nfs at different concentrations was added to the well, and the mixture was incubated at 37 °C for 1 h. The fluorescence intensity was measured under a microplate reader (Tecan, Männedorf, Switzerland) with the excitation and emission wavelengths at 480 and 520 nm, respectively.

To evaluate the cfDNA scavenging activity of Mn_3O_4 Nfs in vivo, peripheral blood of mice was collected from the eyeball. Then, the blood samples were centrifuged at 400 × g for 10 min at 4 °C to obtain the plasma fraction, which was then re-centrifuged at 12,000 × g for 10 min at 4 °C to remove cell debris. The supernatant was isolated carefully and stored at −80 °C. The circulating cfDNA in serum was extracted by using the DNeasy Blood & Tissue Kit. The concentrations of cfDNA in different groups were measured by the Quant-iT PicoGreen dsDNA Reagent and Kits.

To evaluate the level of cfDNA in urine, urine was collected and centrifuged at 1600 × g for 10 min at 4 °C, and then another centrifugation was performed at 16,000 × g for 10 min at 4 °C. The urine samples were stored at −80 °C. The cfDNA in urine was extracted by using the DNeasy Blood & Tissue Kit. The concentrations of cfDNA in different groups were measured by the Quant-iT PicoGreen dsDNA Reagent and Kits.

Assessment of Renal Function. In the IR-AKI mouse model, the left kidney blood vessel was blocked for 45 min, and the right kidney was resected after releasing the left blood vessel clamp. Blood samples were harvested at 48 h in the cisplatin-induced AKI model and at 24 h in the IR-AKI model and were anticoagulated with heparin immediately. The serum was obtained by centrifuging blood samples at 3000 rpm for 15 min at 4 °C and was used to measure BUN and blood creatinine levels with the QuantiChrom Urea Assay Kit and QuantiChrom Creatinine Assay Kit, respectively. All tests were performed following the protocols provided by the manufacturers.

In Vivo MRI in the Cisplatin-Induced AKI Model. A Bruker BioSpec 94/20 small animal MR system (Bruker BioSpin MRI, Ettlingen, Germany) operating at 400 MHz (9.4 Tesla) was used to measure the accumulation of Mn_3O_4 Nfs in kidneys. Twenty-four hours after intraperitoneal injection of cisplatin or PBS, both AKI mice and healthy mice were anesthetized with isoflurane inhalation and were in vivo imaged with T_1-weighted MRI for "0 h" MRI images. After the mice woke up, they were iv injected with Mn_3O_4 Nfs (10 mg/kg). Subsequently, MRI was performed on mice at different time

https://doi.org/10.1021/acsami.2c16305
ACS Appl. Mater. Interfaces 2022, 14, 50649−50663

points (1, 3, 6, 12, 24, and 48 h) after Mn_3O_4 Nf injection. MRI signals were quantified, and MRI images were processed with ITK-SNAP.

In Vivo Biocompatibility of Mn_3O_4 Nfs. Healthy mice and AKI mice were iv injected with PBS or a series of doses of Mn_3O_4 Nfs (5, 10, and 20 mg/kg). Blood samples were harvested to evaluate liver/kidney function (ALT, AST, BUN, creatinine) and inflammatory cytokines (IL-6, IL-1β, and TNF-α).

H&E staining was used to evaluate the safety of Mn_3O_4 Nfs for major organs in vivo. Healthy ICR mice were iv injected with PBS or 10 mg/kg Mn_3O_4 Nfs. Then, major organs (heart, liver, spleen, lung, and kidney) were harvested at 24 h (short-term) and 1 month (long-term) for H&E analysis.

Statistical Analysis. Statistical analysis involved two-sided Student's *t*-test for two groups and one-way ANOVA for multiple groups. $P < 0.05$ was considered statistically significant.

■ ASSOCIATED CONTENT

Supporting Information

The Supporting Information is available free of charge at https://pubs.acs.org/doi/10.1021/acsami.2c16305.

Zeta potential and XPS analysis of Mn_3O_4 Nfs; SOD- and CAT-like activities of Mn_3O_4 Nps and Mn_3O_4 Nfs; •OH scavenging ability and cfDNA adsorption by gel electrophoresis analysis for Mn_3O_4 Nfs; cfDNA adsorption ability of MSN; dispersion stability of Mn_3O_4 Nfs; cellular toxicity and ROS-scavenging activity of Mn_3O_4 Nps and Mn_3O_4 Nfs; level of cfDNA in urine after different treatments; toxicity of Mn_3O_4 Nfs-cfDNA in vivo; the mRNA levels of KIM-1 and HO-1 and ATP levels in renal tissues; AKI biomarker assessment in the IR model; and in vivo toxicity of Mn_3O_4 Nfs measured by liver/kidney function, inflammatory cytokine levels, and HE staining of major organs (PDF)

■ AUTHOR INFORMATION

Corresponding Authors

Xiaozhi Zhao − *Department of Urology, Nanjing Drum Tower Hospital, The Affiliated Hospital of Nanjing University Medical School, Institute of Urology Nanjing University, Nanjing, Jiangsu 210008, China;* orcid.org/0000-0002-4265-9730; Email: zhaoxz@nju.edu.cn

Hui Wei − *Department of Biomedical Engineering, College of Engineering and Applied Sciences, Nanjing National Laboratory of Microstructures, Jiangsu Key Laboratory of Artificial Functional Materials, Nanjing University, Nanjing, Jiangsu 210093, China; State Key Laboratory of Analytical Chemistry for Life Science, School of Chemistry and Chemical Engineering, Chemistry and Biomedicine Innovation Center (ChemBIC), Nanjing University, Nanjing, Jiangsu 210023, China;* orcid.org/0000-0003-0870-7142; Email: weihui@nju.edu.cn

Hongqian Guo − *Department of Urology, Nanjing Drum Tower Hospital, The Affiliated Hospital of Nanjing University Medical School, Institute of Urology Nanjing University, Nanjing, Jiangsu 210008, China;* orcid.org/0000-0002-3121-5157; Email: dr.ghq@nju.edu.cn

Authors

Longxiyu Meng − *Department of Urology, Nanjing Drum Tower Hospital, The Affiliated Hospital of Nanjing University Medical School, Institute of Urology Nanjing University, Nanjing, Jiangsu 210008, China*

Jiayuan Feng − *Department of Biomedical Engineering, College of Engineering and Applied Sciences, Nanjing National Laboratory of Microstructures, Jiangsu Key Laboratory of Artificial Functional Materials, Nanjing University, Nanjing, Jiangsu 210093, China*

Jie Gao − *Department of Urology, Nanjing Drum Tower Hospital, The Affiliated Hospital of Nanjing University Medical School, Institute of Urology Nanjing University, Nanjing, Jiangsu 210008, China*

Yihong Zhang − *Department of Biomedical Engineering, College of Engineering and Applied Sciences, Nanjing National Laboratory of Microstructures, Jiangsu Key Laboratory of Artificial Functional Materials, Nanjing University, Nanjing, Jiangsu 210093, China*

Wenjing Mo − *Department of Urology, Nanjing Drum Tower Hospital, The Affiliated Hospital of Nanjing University of Chinese Medicine, Nanjing, Jiangsu 210008, China*

Complete contact information is available at: https://pubs.acs.org/10.1021/acsami.2c16305

Author Contributions

L.M., J.F., and J.G. contributed equally to this work. H.W., X.Z., and L.M. designed the study. J.F. designed and synthesized the materials and performed the material characterization experiment. L.M. and J.G. designed and performed the in vitro and in vivo studies. Y.Z. assisted with the material characterization experiment. W.M. assisted with the in vitro and in vivo studies. The manuscript was written through contributions of all authors. All authors have given approval to the final version of the manuscript.

Funding

This work was supported by the National Natural Science Foundation of China (81772710, 81972388, 82070703, 82103002, 92168112, and 21874067), the China Postdoctoral Science Foundation (2022 M711579), and the National Key R&D Program of China (2019YFA0709200 and 2021YFF1200700).

Notes

The authors declare no competing financial interest.

$^{\perp}$L.M., J.F., and J.G. are co-first authors.

■ ACKNOWLEDGMENTS

We thank Dr. Min Zhou for her help with the experiment and discussion.

■ REFERENCES

(1) Levey, A. S.; James, M. T. Acute Kidney Injury. *Ann. Intern. Med.* **2017**, *167*, ITC66−ITC80.

(2) Ronco, C.; Bellomo, R.; Kellum, J. A. Acute Kidney Injury. *Lancet* **2019**, *394*, 1949−1964.

(3) Hoste, E. A.; Bagshaw, S. M.; Bellomo, R.; Cely, C. M.; Colman, R.; Cruz, D. N.; Edipidis, K.; Forni, L. G.; Gomersall, C. D.; Govil, D.; Honore, P. M.; Joannes-Boyau, O.; Joannidis, M.; Korhonen, A. M.; Lavrentieva, A.; Mehta, R. L.; Palevsky, P.; Roessler, E.; Ronco, C.; Uchino, S.; Vazquez, J. A.; Vidal Andrade, E.; Webb, S.; Kellum, J. A. Epidemiology of Acute Kidney Injury in Critically Ill Patients: the Multinational AKI-EPI Study. *Intensive Care Med.* **2015**, *41*, 1411−1423.

(4) Guo, C.; Dong, G.; Liang, X.; Dong, Z. Epigenetic Regulation in AKI and Kidney Repair: Mechanisms and Therapeutic Implications. *Nat. Rev. Nephrol.* **2019**, *15*, 220−239.

(5) Lameire, N. H.; Bagga, A.; Cruz, D.; De Maeseneer, J.; Endre, Z.; Kellum, J. A.; Liu, K. D.; Mehta, R. L.; Pannu, N.; Van Biesen, W.;

Vanholder, R. Acute Kidney Injury: an Increasing Global Concern. *Lancet* **2013**, *382*, 170−179.
(6) Gonsalez, S. R.; Cortes, A. L.; Silva, R. C. D.; Lowe, J.; Prieto, M. C.; Silva Lara, L. D. Acute Kidney Injury Overview: From Basic Findings to New Prevention and Therapy Strategies. *Pharmacol. Ther.* **2019**, *200*, 1−12.
(7) Fu, Z. J.; Wang, Z. Y.; Xu, L.; Chen, X. H.; Li, X. X.; Liao, W. T.; Ma, H. K.; Jiang, M. D.; Xu, T. T.; Xu, J.; Shen, Y.; Song, B.; Gao, P. J.; Han, W. Q.; Zhang, W. HIF-1alpha-BNIP3-Mediated Mitophagy in Tubular Cells Protects against Renal Ischemia/Reperfusion Injury. *Redox Biol.* **2020**, *36*, No. 101671.
(8) Meng, X. M.; Ren, G. L.; Gao, L.; Yang, Q.; Li, H. D.; Wu, W. F.; Huang, C.; Zhang, L.; Lv, X. W.; Li, J. NADPH Oxidase 4 Promotes Cisplatin-Induced Acute Kidney Injury via ROS-Mediated Programmed Cell Death and Inflammation. *Lab. Invest.* **2018**, *98*, 63−78.
(9) Poston, J. T.; Koyner, J. L. Sepsis Associated Acute Kidney Injury. *BMJ* **2019**, *364*, k4891.
(10) Zhao, M.; Wang, Y.; Li, L.; Liu, S.; Wang, C.; Yuan, Y.; Yang, G.; Chen, Y.; Cheng, J.; Lu, Y.; Liu, J. Mitochondrial ROS Promote Mitochondrial Dysfunction and Inflammation in Ischemic Acute Kidney Injury by Disrupting TFAM-Mediated mtDNA Maintenance. *Theranostics* **2021**, *11*, 1845−1863.
(11) Mittler, R. ROS Are Good. *Trends Plant Sci.* **2017**, *22*, 11−19.
(12) Wang, Y.; Branicky, R.; Noe, A.; Hekimi, S. Superoxide Dismutases: Dual Roles in Controlling ROS Damage and Regulating ROS Signaling. *J. Cell. Biol.* **2018**, *217*, 1915−1928.
(13) Wu, J.; Wang, X.; Wang, Q.; Lou, Z.; Li, S.; Zhu, Y.; Qin, L.; Wei, H. Nanomaterials with Enzyme-like Characteristics (Nanozymes): Next-Generation Artificial Enzymes (II). *Chem. Soc. Rev.* **2019**, *48*, 1004−1076.
(14) Wei, H.; Wang, E. Nanomaterials with Enzyme-like Characteristics (Nanozymes): Next-Generation Artificial Enzymes. *Chem. Soc. Rev.* **2013**, *42*, 6060−6093.
(15) Zhang, R.; Yan, X.; Fan, K. Nanozymes Inspired by Natural Enzymes. *Acc. Mater. Res.* **2021**, *2*, 534−547.
(16) Liang, M.; Yan, X. Nanozymes: From New Concepts, Mechanisms, and Standards to Applications. *Acc. Chem. Res.* **2019**, *52*, 2190−2200.
(17) Huang, Y.; Ren, J.; Qu, X. Nanozymes: Classification, Catalytic Mechanisms, Activity Regulation, and Applications. *Chem. Rev.* **2019**, *119*, 4357−4412.
(18) Zhou, Y.; Liu, B.; Yang, R.; Liu, J. Filling in the Gaps between Nanozymes and Enzymes: Challenges and Opportunities. *Bioconjugate Chem.* **2017**, *28*, 2903−2909.
(19) Dong, H.; Fan, Y.; Zhang, W.; Gu, N.; Zhang, Y. Catalytic Mechanisms of Nanozymes and Their Applications in Biomedicine. *Bioconjugate Chem.* **2019**, *30*, 1273−1296.
(20) Ragg, R.; Tahir, M. N.; Tremel, W. Solids Go Bio: Inorganic Nanoparticles as Enzyme Mimics. *Eur. J. Inorg. Chem.* **2016**, *2016*, 1896−1896.
(21) Gao, L.; Zhuang, J.; Nie, L.; Zhang, J.; Zhang, Y.; Gu, N.; Wang, T.; Feng, J.; Yang, D.; Perrett, S.; Yan, X. Intrinsic Peroxidase-like Activity of Ferromagnetic Nanoparticles. *Nat. Nanotechnol.* **2007**, *2*, 577−583.
(22) Manea, F.; Houillon, F. B.; Pasquato, L.; Scrimin, P. Nanozymes: Gold-Nanoparticle-Based Transphosphorylation Catalysts. *Angew. Chem., Int. Ed.* **2004**, *43*, 6165−6169.
(23) Komkova, M. A.; Karyakina, E. E.; Karyakin, A. A. Catalytically Synthesized Prussian Blue Nanoparticles Defeating Natural Enzyme Peroxidase. *J. Am. Chem. Soc.* **2018**, *140*, 11302−11307.
(24) Huang, L.; Chen, J.; Gan, L.; Wang, J.; Dong, S. Single-Atom Nanozymes. *Sci. Adv.* **2019**, *5*, No. eaav5490.
(25) Chen, J.; Patil, S.; Seal, S.; McGinnis, J. F. Rare Earth Nanoparticles Prevent Retinal Degeneration Induced by Intracellular Peroxides. *Nat. Nanotechnol.* **2006**, *1*, 142−150.
(26) Wang, Q.; Cheng, C.; Zhao, S.; Liu, Q.; Zhang, Y.; Liu, W.; Zhao, X.; Zhang, H.; Pu, J.; Zhang, S.; Zhang, H.; Du, Y.; Wei, H. A. Valence-Engineered Self-Cascading Antioxidant Nanozyme for the Therapy of Inflammatory Bowel Disease. *Angew. Chem., Int. Ed.* **2022**, No. e202201101.
(27) Han, S. I.; Lee, S.-W.; Cho, M. G.; Yoo, J. M.; Oh, M. H.; Jeong, B.; Kim, D.; Park, O. K.; Kim, J.; Namkoong, E.; Jo, J.; Lee, N.; Lim, C.; Soh, M.; Sung, Y.-E.; Yoo, J.; Park, K.; Hyeon, T. Epitaxially Strained CeO /MnO Nanocrystals as an Enhanced Antioxidant for Radioprotection. *Adv. Mater.* **2020**, *32*, No. e2001566.
(28) Wu, H.; Xia, F.; Zhang, L.; Fang, C.; Lee, J.; Gong, L.; Gao, J.; Ling, D.; Li, F. A ROS-Sensitive Nanozyme-Augmented Photoacoustic Nanoprobe for Early Diagnosis and Therapy of Acute Liver Failure. *Adv. Mater.* **2022**, *34*, No. e2108348.
(29) Jiang, D.; Rosenkrans, Z. T.; Ni, D.; Lin, J.; Huang, P.; Cai, W. Nanomedicines for Renal Management: From Imaging to Treatment. *Acc. Chem. Res.* **2020**, *53*, 1869−1880.
(30) Jiang, D.; Ni, D.; Rosenkrans, Z. T.; Huang, P.; Yan, X.; Cai, W. Nanozyme: New Horizons for Responsive Biomedical Applications. *Chem. Soc. Rev.* **2019**, *48*, 3683−3704.
(31) Liu, Z.; Xie, L.; Qiu, K.; Liao, X.; Rees, T. W.; Zhao, Z.; Ji, L.; Chao, H. An Ultrasmall RuO2 Nanozyme Exhibiting Multienzyme-like Activity for the Prevention of Acute Kidney Injury. *ACS Appl. Mater. Interfaces* **2020**, *12*, 31205−31216.
(32) Zhang, D. Y.; Liu, H.; Li, C.; Younis, M. R.; Lei, S.; Yang, C.; Lin, J.; Li, Z.; Huang, P. Ceria Nanozymes with Preferential Renal Uptake for Acute Kidney Injury Alleviation. *ACS Appl. Mater. Interfaces* **2020**, *12*, 56830−56838.
(33) Zhang, D. Y.; Younis, M. R.; Liu, H.; Lei, S.; Wan, Y.; Qu, J.; Lin, J.; Huang, P. Multi-Enzyme Mimetic Ultrasmall Iridium Nanozymes as Reactive Oxygen/Nitrogen Species Scavengers for Acute Kidney Injury Management. *Biomaterials* **2021**, *271*, No. 120706.
(34) Zhang, D.-Y.; Liu, H.; Zhu, K. S.; He, T.; Younis, M. R.; Yang, C.; Lei, S.; Wu, J.; Lin, J.; Qu, J.; Huang, P. Prussian Blue-Based Theranostics for Ameliorating Acute Kidney Injury. *J. Nanobiotechnology* **2021**, *19*, 266.
(35) Zhang, D.-Y.; Tu, T.; Younis, M. R.; Zhu, K. S.; Liu, H.; Lei, S.; Qu, J.; Lin, J.; Huang, P. Clinically Translatable Gold Nanozymes with Broad Spectrum Antioxidant and Anti-Inflammatory Activity for Alleviating Acute Kidney Injury. *Theranostics* **2021**, *11*, 9904−9917.
(36) Zhang, D.-Y.; Liu, H.; Rizwan Younis, M.; Lei, S.; Yang, C.; Lin, J.; Qu, J.; Huang, P. Ultrasmall Platinum Nanozymes as Broad-Spectrum Antioxidants for Theranostic Application in Acute Kidney Injury. *Chem. Eng. J.* **2021**, *421*, No. 129963.
(37) Homolova, J.; Janovicova, L.; Konecna, B.; Vlkova, B.; Celec, P.; Tothova, L.; Babickova, J. Plasma Concentrations of Extracellular DNA in Acute Kidney Injury. *Diagnostics* **2020**, *10*, 152.
(38) Gong, W.; Lu, L.; Zhou, Y.; Liu, J.; Ma, H.; Fu, L.; Huang, S.; Zhang, Y.; Zhang, A.; Jia, Z. The Novel STING Antagonist H151 Ameliorates Cisplatin-Induced Acute Kidney Injury and Mitochondrial Dysfunction. *Am. J. Physiol. Renal Physiol.* **2021**, *320*, F608−F616.
(39) Iske, J.; Seyda, M.; Heinbokel, T.; Maenosono, R.; Minami, K.; Nian, Y.; Quante, M.; Falk, C. S.; Azuma, H.; Martin, F.; Passos, J. F.; Niemann, C. U.; Tchkonia, T.; Kirkland, J. L.; Elkhal, A.; Tullius, S. G. Senolytics Prevent mt-DNA-Induced Inflammation and Promote the Survival of Aged Organs Following Transplantation. *Nat. Commun.* **2020**, *11*, 4289.
(40) Tian, Y.; Charles, E. J.; Yan, Z.; Wu, D.; French, B. A.; Kron, I. L.; Yang, Z. The Myocardial Infarct-Exacerbating Effect of Cell-Free DNA Is Mediated by the High-Mobility Group Box 1-Receptor for Advanced Glycation End Products-Toll-like Receptor 9 Pathway. *J. Thorac. Cardiovasc. Surg.* **2019**, *157*, 2256.
(41) Grosse, G. M.; Blume, N.; Abu-Fares, O.; Götz, F.; Ernst, J.; Leotescu, A.; Gabriel, M. M.; van Gemmeren, T.; Worthmann, H.; Lichtinghagen, R.; Imker, R.; Falk, C. S.; Weissenborn, K.; Schuppner, R.; de Buhr, N. Endogenous Deoxyribonuclease Activity and Cell-Free Deoxyribonucleic Acid in Acute Ischemic Stroke: A Cohort Study. *Stroke* **2022**, *53*, 1235−1244.
(42) Dawulieti, J.; Sun, M.; Zhao, Y.; Shao, D.; Yan, H.; Lao, Y.-H.; Hu, H.; Cui, L.; Lv, X.; Liu, F.; Chi, C.-W.; Zhang, Y.; Li, M.; Zhang,

https://doi.org/10.1021/acsami.2c16305
ACS Appl. Mater. Interfaces 2022, 14, 50649−50663

M.; Tian, H.; Chen, X.; Leong, K. W.; Chen, L. Treatment of Severe Sepsis with Nanoparticulate Cell-Free DNA Scavengers. *Sci. Adv.* **2020**, *6*, No. eaay7148.
(43) Celec, P.; Vlkova, B.; Laukova, L.; Babickova, J.; Boor, P. Cell-Free DNA: the Role in Pathophysiology and as a Biomarker in Kidney Diseases. *Expert. Rev. Mol. Med.* **2018**, *20*, No. e1.
(44) Shmarina, G. V.; Ershova, E. S.; Simashkova, N. V.; Nikitina, S. G.; Chudakova, J. M.; Veiko, N. N.; Porokhovnik, L. N.; Basova, A. Y.; Shaposhnikova, A. F.; Pukhalskaya, D. A.; Pisarev, V. M.; Korovina, N. J.; Gorbachevskaya, N. L.; Dolgikh, O. A.; Bogush, M.; Kutsev, S. I.; Kostyuk, S. V. Oxidized Cell-Free DNA as a Stress-Signaling Factor Activating the Chronic Inflammatory Process in Patients with Autism Spectrum Disorders. *J. Neuroinflammation* **2020**, *17*, 212.
(45) Andargie, T. E.; Tsuji, N.; Seifuddin, F.; Jang, M. K.; Yuen, P. S.; Kong, H.; Tunc, I.; Singh, K.; Charya, A.; Wilkins, K.; Nathan, S.; Cox, A.; Pirooznia, M.; Star, R. A.; Agbor-Enoh, S. Cell-Free DNA Maps COVID-19 Tissue Injury and Risk of Death and Can Cause Tissue Injury. *JCI Insight* **2021**, *6*, No. e147610.
(46) Tsuji, N.; Tsuji, T.; Ohashi, N.; Kato, A.; Fujigaki, Y.; Yasuda, H. Role of Mitochondrial DNA in Septic AKI via Toll-Like Receptor 9. *J. Am. Soc. Nephrol.* **2016**, *27*, 2009−2020.
(47) Ermakov, A. V.; Konkova, M. S.; Kostyuk, S. V.; Izevskaya, V. L.; Baranova, A.; Veiko, N. N. Oxidized Extracellular DNA as a Stress Signal in Human Cells. *Oxid. Med. Cell. Longevity* **2013**, *2013*, No. 649747.
(48) Zhou, M.; Wang, X.; Lin, S.; Cheng, Y.; Zhao, S.; Lin, J.; Fang, Z.; Lou, Z.; Qin, L.; Wei, H. Multifunctional STING-Activating Mn_3O_4 @Au-dsDNA/DOX Nanoparticle for Antitumor Immunotherapy. *Adv. Healthcare Mater.* **2020**, *9*, No. e2000064.
(49) Singh, N.; Savanur, M. A.; Srivastava, S.; D'Silva, P.; Mugesh, G. A Redox Modulatory Mn_3O_4 Nanozyme with Multi-Enzyme Activity Provides Efficient Cytoprotection to Human Cells in a Parkinson's Disease Model. *Angew. Chem., Int. Ed.* **2017**, *56*, 14267−14271.
(50) Yao, J.; Cheng, Y.; Zhou, M.; Zhao, S.; Lin, S.; Wang, X.; Wu, J.; Li, S.; Wei, H. ROS Scavenging Mn_3O_4 Nanozymes for in vivo Anti-Inflammation. *Chem. Sci.* **2018**, *9*, 2927−2933.
(51) Cheng, Y.; Cheng, C.; Yao, J.; Yu, Y.; Liu, Y.; Zhang, H.; Miao, L.; Wei, H. Mn_3O_4 Nanozyme for Inflammatory Bowel Disease Therapy. *Adv. Ther.* **2021**, *4*, 2100081.
(52) Singh, N.; Geethika, M.; Eswarappa, S. M.; Mugesh, G. Manganese-Based Nanozymes: Multienzyme Redox Activity and Effect on the Nitric Oxide Produced by Endothelial Nitric Oxide Synthase. *Chemistry* **2018**, *24*, 8393−8403.
(53) Jančuška, A.; Potočárová, A.; Kovalčíková, A. G.; Podracká, L'.; Bábíčková, J.; Celec, P.; Tóthová, L'. Dynamics of Plasma and Urinary Extracellular DNA in Acute Kidney Injury. *Int. J. Mol. Sci.* **2022**, *23*, 3402.
(54) Herrera, C. A.; Stoerker, J.; Carlquist, J.; Stoddard, G. J.; Jackson, M.; Esplin, S.; Rose, N. C. Cell-Free DNA, Inflammation, and the Initiation of Spontaneous Term Labor. *Am. J. Obstet. Gynecol.* **2017**, *217*, 583.e581−583.e588.
(55) Mao, X.; Yu, C. R.; Li, W. H.; Li, W. X. Induction of Apoptosis by Shikonin through a ROS/JNK-Mediated Process in Bcr/Abl-Positive Chronic Myelogenous Leukemia (CML) Cells. *Cell Res.* **2008**, *18*, 879−888.
(56) Lee, M. Y.; Jung, S. C.; Lee, J. H.; Han, H. J. Estradiol-17beta Protects against Hypoxia-Induced Hepatocyte Injury through ER-Mediated Upregulation of Bcl-2 as well as ER-Independent Antioxidant Effects. *Cell Res.* **2008**, *18*, 491−499.
(57) Hamroun, A.; Lenain, R.; Bigna, J. J.; Speyer, E.; Bui, L.; Chamley, P.; Pottier, N.; Cauffiez, C.; Dewaeles, E.; Dhalluin, X.; Scherpereel, A.; Hazzan, M.; Maanaoui, M.; Glowacki, F. Prevention of Cisplatin-Induced Acute Kidney Injury: A Systematic Review and Meta-Analysis. *Drugs* **2019**, *79*, 1567−1582.
(58) Miller, R. P.; Tadagavadi, R. K.; Ramesh, G.; Reeves, W. B. Mechanisms of Cisplatin Nephrotoxicity. *Toxins* **2010**, *2*, 2490−2518.
(59) Li, X.; Pan, J.; Li, H.; Li, G.; Liu, X.; Liu, B.; He, Z.; Peng, Z.; Zhang, H.; Li, Y.; Xiang, X.; Chai, X.; Yuan, Y.; Zheng, P.; Liu, F.; Zhang, D. DsbA-L Mediated Renal Tubulointerstitial Fibrosis in UUO Mice. *Nat. Commun.* **2020**, *11*, 4467.
(60) Chung, K. W.; Dhillon, P.; Huang, S.; Sheng, X.; Shrestha, R.; Qiu, C.; Kaufman, B. A.; Park, J.; Pei, L.; Baur, J.; Palmer, M.; Susztak, K. Mitochondrial Damage and Activation of the STING Pathway Lead to Renal Inflammation and Fibrosis. *Cell Metab.* **2019**, *30*, 784−799.e5. e785
(61) Chawla, L. S.; Eggers, P. W.; Star, R. A.; Kimmel, P. L. Acute Kidney Injury and Chronic Kidney Disease as Interconnected Syndromes. *N. Engl. J. Med.* **2014**, *371*, 58−66.
(62) Murugan, R.; Kellum, J. A. Acute Kidney Injury: What's the Prognosis? *Nat. Rev. Nephrol.* **2011**, *7*, 209−217.
(63) Hapca, S.; Siddiqui, M. K.; Kwan, R. S. Y.; Lim, M.; Matthew, S.; Doney, A. S. F.; Pearson, E. R.; Palmer, C. N. A.; Bell, S. The Relationship between AKI and CKD in Patients with Type 2 Diabetes: An Observational Cohort Study. *J. Am. Soc. Nephrol.* **2021**, *32*, 138−150.
(64) Wolyniec, W.; Ratkowski, W.; Renke, J.; Renke, M. Changes in Novel AKI Biomarkers after Exercise. A Systematic Review. *Int. J. Mol. Sci.* **2020**, *21*, 5673.
(65) Shang, W.; Wang, Z. The Update of NGAL in Acute Kidney Injury. *Curr. Protein Pept. Sci.* **2017**, *18*, 1211−1217.
(66) Bonventre, J. V. Kidney Injury Molecule-1 (KIM-1): A Urinary Biomarker and Much More. *Nephrol. Dial Transplant* **2009**, *24*, 3265−3268.
(67) Zager, R. A.; Johnson, A. C.; Becker, K. Plasma and Urinary Heme Oxygenase-1 in AKI. *J. Am. Soc. Nephrol.* **2012**, *23*, 1048−1057.
(68) Lei, G.; Zhang, Y.; Koppula, P.; Liu, X.; Zhang, J.; Lin, S. H.; Ajani, J. A.; Xiao, Q.; Liao, Z.; Wang, H.; Gan, B. The Role of Ferroptosis in Ionizing Radiation-Induced Cell Death and Tumor Suppression. *Cell Res.* **2020**, *30*, 146−162.
(69) Deng, F.; Sharma, I.; Dai, Y.; Yang, M.; Kanwar, Y. S. Myo-Inositol Oxygenase Expression Profile Modulates Pathogenic Ferroptosis in the Renal Proximal Tubule. *J. Clin. Invest.* **2019**, *129*, 5033−5049.
(70) Stockwell, B. R.; Friedmann Angeli, J. P.; Bayir, H.; Bush, A. I.; Conrad, M.; Dixon, S. J.; Fulda, S.; Gascon, S.; Hatzios, S. K.; Kagan, V. E.; Noel, K.; Jiang, X.; Linkermann, A.; Murphy, M. E.; Overholtzer, M.; Oyagi, A.; Pagnussat, G. C.; Park, J.; Ran, Q.; Rosenfeld, C. S.; Salnikow, K.; Tang, D.; Torti, F. M.; Torti, S. V.; Toyokuni, S.; Woerpel, K. A.; Zhang, D. D. Ferroptosis: A Regulated Cell Death Nexus Linking Metabolism, Redox Biology, and Disease. *Cell* **2017**, *171*, 273−285.
(71) Tsikas, D. Assessment of Lipid Peroxidation by Measuring Malondialdehyde (MDA) and Relatives in Biological Samples: Analytical and Biological Challenges. *Anal. Biochem.* **2017**, *524*, 13−30.
(72) Rovcanin, B.; Medic, B.; Kocic, G.; Cebovic, T.; Ristic, M.; Prostran, M. Molecular Dissection of Renal Ischemia-Reperfusion: Oxidative Stress and Cellular Events. *Curr. Med. Chem.* **2016**, *23*, 1965−1980.
(73) Diao, C.; Chen, Z.; Qiu, T.; Liu, H.; Yang, Y.; Liu, X.; Wu, J.; Wang, L. Inhibition of PRMT5 Attenuates Oxidative Stress-Induced Pyroptosis via Activation of the Nrf2/HO-1 Signal Pathway in a Mouse Model of Renal Ischemia-Reperfusion Injury. *Oxid. Med. Cell. Longevity* **2019**, *2019*, 2345658.
(74) Yu, H.; Lin, T.; Chen, W.; Cao, W.; Zhang, C.; Wang, T.; Ding, M.; Zhao, S.; Wei, H.; Guo, H.; Zhao, X. Size and Temporal-Dependent Efficacy of Oltipraz-Loaded PLGA Nanoparticles for Treatment of Acute Kidney Injury and Fibrosis. *Biomaterials* **2019**, *219*, No. 119368.
(75) Tampe, B.; Steinle, U.; Tampe, D.; Carstens, J. L.; Korsten, P.; Zeisberg, E. M.; Müller, G. A.; Kalluri, R.; Zeisberg, M. Low-Dose Hydralazine Prevents Fibrosis in a Murine Model of Acute Kidney Injury-to-Chronic Kidney Disease Progression. *Kidney Int.* **2017**, *91*, 157−176.

https://doi.org/10.1021/acsami.2c16305
ACS Appl. Mater. Interfaces 2022, 14, 50649−50663

(76) Gou, H.; Liu, Y.; Zhang, G.; Liao, Q.; Huang, X.; Ning, F.; Ke, C.; Meng, Z.; Xi, K. Lifetime-Tunable Room-Temperature Phosphorescence of Polyaniline Carbon Dots in Adjustable Polymer Matrices. *Nanoscale* **2019**, *11*, 18311−18319.
(77) Chen, W.; Yuan, H.; Cao, W.; Wang, T.; Chen, W.; Yu, H.; Fu, Y.; Jiang, B.; Zhou, H.; Guo, H.; Zhao, X. Blocking Interleukin-6 Trans-Signaling Protects against Renal Fibrosis by Suppressing STAT3 Activation. *Theranostics* **2019**, *9*, 3980−3991.

https://doi.org/10.1021/acsami.2c16305
ACS Appl. Mater. Interfaces 2022, 14, 50649−50663